Results in Earth Sciences 3 (2025) 100080

Contents lists available at ScienceDirect

Results in Earth Sciences

journal homepage: www.sciencedirect.com/journal/results-in-earth-sciences

Geochemistry of podiform chromitite and host rocks within the Buem Structural Unit, Northwestern Benin Republic: Implications for the geodynamic evolution of the Dahomeyide orogenic belt

Daniel N. Kouagou N'Dah [a,c,*], Samuel B. Olobaniyi [b], Luc C. Adissin Glodji [c], Sory I.M. Konate [a], Elhadji Mory Traore [a], Daniel Kwayisi [d,e], Clement B. N'Satta [c], Ibrahim S. Yerima [c]

[a] Pan African University Life and Earth Sciences Institute (PAULESI), Ibadan, Oyo State, Nigeria
[b] Department of Geosciences, University of Lagos, Lagos, Nigeria
[c] Department of Earth Sciences, University of Abomey-Calavi, Abomey-Calavi, Benin Republic
[d] Department of Geology, University of Johannesburg, Auckland Park Kingsway Campus, South Africa
[e] Department of Earth Sciences, University of Ghana, Legon-Accra, Ghana

ARTICLE INFO

Keywords:
Chromitite
Dahomeyide orogenic belt
Podiform
Ophiolite
Geodynamic
Benin

ABSTRACT

The paper presents the geochemistry, origin and geodynamic setting of podiform chromitite and host rocks from the Buem Structural Unit (BSU) in the northwestern Benin Republic. Qualitative Scanning Electron Microscopy (SEM), quantitative Electron probe Micro Analysis (EPMA), and whole-rock geochemical investigation have been conducted on BSU chromite and mafic-ultramafic rocks. The BSU is the westernmost unit of the Dahomeyide orogenic belt. It consists mainly of metamorphosed mafic-ultramafic rock and clastic sedimentary rocks. Chromitites units are exposed within the mafic-ultramafic rocks. Qualitative SEM analyses indicated that chromitite is mainly composed of chromite and serpentine minerals. The qualitative EPMA data shows that Cr_2O_3 and MnO contents (wt%) of spinel of the BSU varying from 35.91 to 44.53 and from 0.05 to 0.16, respectively and are typical primary Cr-spinel. The calculated parental composition of melts (13.71–16.67 wt% Al_2O_3 and FeO/MgO values in the range 0.15–0.30) from which the BSU chromitites precipitated is very similar to MORB-type magma. The chemical composition of BSU chromites and its host rocks shows that these chromites were most likely crystallized from MORB. The magma originated as a partial melt that occurred in a Mid Ocean Ridge environment, probably during the early stage of the Pan-African orogeny at the margin of the West African Craton.

1. Introduction

Chromite is an accessory mineral in mafic-ultramafic rocks and an essential mineral in chromitites (Tesalina et al., 2003; Arif and Qasim Jan, 2006; Malkani et al., 2016; Mekhonoshin et al., 2020). It is a chrome spinel mineral group having the chemical formula ((Fe, Mg), (Al Cr)$_2$O$_4$). Several studies have highlighted the significance of mafic and ultramafic hosted chromite minerals in tectonic and petrogenetic interpretations (Irvine, 1965; Barnes, 2000; Kamenetsky et al., 2001; Rollinson, 2008; González-Jiménez et al., 2014; Jiang et al., 2024; Zhou et al., 2014). Furthermore, its compositions can give constraints on the degree of mantle partial melting, nature of parental melt, crystallization temperature and fugacity of parental melt (Irvine, 1967; Dick & Bullen, 1984; Scowen et al., 1991; Arai, 1992; Arai & Yurimoto, 1994; Uysal et al., 2009; Mukherjee et al., 2010; Zaccarini et al., 2011; Zhou et al., 2014).

The chromite deposits are generally grouped into two types according to their geological setting and occurrences: podiform chromite and stratiform/layered chromite (Stowe, 1994; Paktunc, 1990). Podiform chromites mainly occur in ophiolites or mantle peridotites (Dick, 1977; Yang et al., 2022). The Kempirsai chromite deposit (Kazakhstan), the Ray-Iz chromite deposit from the Polar Urals and the Luobusha chromite deposit in Xizang (China) are typical podiform chromite deposits (Melcher et al., 1997; Uysal et al., 2009; Yang et al., 2015). The molar ratio of chromite defined as {Cr# = Cr/(Cr + Al)}, has been used to describe the composition of chromitite. Podiform chromitite shows

* Corresponding author at: Pan African University Life and Earth Sciences Institute (PAULESI), Ibadan, Oyo State, Nigeria.
E-mail address: ntchadan.kouagoundah@gmail.com (D.N. Kouagou N'Dah).

https://doi.org/10.1016/j.rines.2025.100080
Received 7 November 2024; Received in revised form 4 March 2025; Accepted 4 March 2025
Available online 8 March 2025

two main compositional varieties of the Cr# (Zhou et al., 1994, 1998; Ahmed and Arai, 2002). Low-Cr# (40−60) varieties are attributed to the passage of relatively Cr-poor MORB magma through the upper mantle during the initial formation of the ophiolite crust (most likely in a back-arc rift setting) while high-Cr# podiform chromitites (70–80) are attributed to the passage through the upper mantle of highly magnesian magmas such as bonitite. The two varieties may occur in the same ophiolite complex (Zhou et al., 1994, 1998; Ahmed and Arai, 2002; Miura et al., 2012).

Stratiform chromite deposits occur within stable cratons or continental margins and are distributed in layered mafic-ultramafic complexes, and chromite ore beds are often interbedded with silicate rock layers (Xiong et al., 2023). Typical examples include Bushveld in South Africa (Maier et al., 2015; Latypov et al., 2017), Stillwater in the United States (Campbell and Murck 1993; Spandler et al., 2005), and Great Dyke in Zimbabwe (Maier et al., 2015).

In the Buem Structural Unit (BSU) of the Dahomeyide orogenic belt, chromitite bodies outcrop within metamorphosed mafic-ultramafic rocks (Affaton et al., 1997; Glodji et al., 2019). However, very little information is available concerning the geochemistry and petrogenesis of these pods chromitite bodies and host rock (metabasalt and serpentinite). Consequently, the origin and tectonic setting of the chromite deposits in the belt are poorly constrained. In this paper, we present the geochemical and mineralogical data on the chromite deposits of the BSU, NW Benin Republic and discusses its tectonic and petrogenetic implications for the BSU and Dohomeyide orogenic belt.

2. Geology setting

The West African Craton (WAC) is mostly surrounded by the Neoproterozoic Pan-African orogenic belts (Attoh, 1998). Among these is the Trans-Saharan and Dohomeyide belts occurring to the east of the Craton (Fig. 1, Affaton et al., 1991; Black et al., 1994; Attoh and Nude, 2008; Kwayisi et al., 2022a, 2023). The Dahomeyide orogen has been interpreted to have originated via the eastward subduction of Neoproterozoic passive margin sequences and Pharusian oceanic crust, and subsequent collision of the WAC with the Benino-Nigerian Shield (BNS) (Attoh, 1998; Castaing et al., 1993; Agbossoumondé et al., 2004; Duclaux et al., 2006; Attoh et al., 2013). From East to West, the Dahomeyide orogenic belt comprises three main units which are in thrust contact and each one constitutes a thrust sheet (Fig. 2): (1) the internal zone consisting of migmatitic granite gneisses (Kalsbeek et al., 2012; Chala et al., 2015; Adissin Glodji et al., 2023); (2) the suture zone, made up of sub-meridian high-pressure and ultra-high pressure metamorphic basic to ultrabasic rocks (Menot, 1980; Attoh, 1998; Attoh and Morgan, 2004; Kwayisi et al., 2022a, 2022b); and (3) the external unit comprises Paleoproterozoic orthogneisses known as Palime-Amlame and Kara pluton in Togo and Ho-gneisses in Ghana (Agbossoumondé et al., 2007; Aidoo et al., 2020) and their Neoproterozoic cover sequences of Buem and Atacora (Togo) structural units (Affaton et al., 1997; Kwayisi et al., 2022b). According to Agbossoumondé et al. (2004, 2007), this unit represents the accretionary prism from the Neoproterozoic overlapping the WAC. The Buem Structural Unit contains chromite deposits (Glodji et al., 2019).

The study area lies within the Buem Structural Unit in the Northwestern Benin Republic. The lithological units within the area consist of the intercalation of south-eastward dipping slightly metamorphosed clastic-chemical sedimentary and volcanic rocks (Affaton, 1990; Jones, 1990; Osae et al., 2006; Kwayisi et al., 2020, 2022b). The clastic sediments include fine-grained sandstone and meta-sandstone, conglomerate, siltstone, shale, and chemical formations are mainly represented by meta-chert or jasper and dolomite. The clastic sedimentary rocks have been subdivided into the lower passive margin and upper active margin sedimentary rocks, with the youngest detrital zircon U-Pb ages of ca. 950 Ma and ca. 600 Ma, respectively (Kalsbeek et al., 2008; Ganade et al., 2016; Kwayisi et al., 2022b). Volcanic rocks of both alkaline and sub-alkaline series, including basalt, dolerite, rhyolite, volcanic breccias and pyroclastic rocks, are interbedded within the sedimentary formations (Affaton, 1990; Affaton et al., 1997; Kwayisi et al., 2022a). The other mafic rock of the BSU is gabbro, which has been well-documented in Ghana (Nude et al., 2015; Kwayisi et al., 2017, 2022a). Podiform chromitite within the BSU has been reported in northwestern Benin by Glodji et al. (2019). Several petrographical and geochemical studies (Affaton et al., 1997; Asiedu et al., 2008; Nude et al., 2015) on the mafic suite and ultramafic complex of the BSU proposed that they formed along the eastern margin of the WAC in an oceanic setting (either mid-oceanic ridge or back-arc). According to Burke et al. (1972), these mafic-ultramafic rocks represent an ophiolite complex, that is the Pharusian oceanic lithosphere that has been obducted during the Pan-African collisional phase. Jones (1990), based on the alkaline nature of the volcanic rocks of BSU proposed an intra-cratonic/continental rift zone. More recently interpretation of lithological associations have inferred that this unit is an ocean-continent transition ophiolite (Kwayisi et al., 2020).

3. Analytical techniques

3.1. SEM analyses

The mineralogical composition of chromitite samples of the Buem Structural Unit was analysed using the TESCAN instrument equipped with Scanning Electron Microscopy (SEM) and Energy Dispersive Spectroscopy (EDS) detectors at both the University of the Witwatersrand and at the University of Johannesburg in South Africa. SEM-EDS analyses were performed on 10 polished thin sections to characterise chromitite petrography and locate mineral inclusions in chromite. Prior to analysis, the polished thin sections were carbon coated to prevent ion buildup (i.e. charging) on the disc surface. The samples were then mounted on an aluminum stub covered with a carbon adhesive. Once placed in the sample holder, the samples were loaded into the small sample chamber to create a vacuum environment (as dust and oxygen can not affect the electron beam) and then loaded into the bigger chamber for analysis. Minerals were located and identified using back-scattered electron (BSE) mode on JEOL JSM 6490LV SEM coupled with Oxford INCA Energy EDS. The microscope was operated using 30 kV for accelerating voltage and 10 nA for the beam current. The field of view was 252 μm × 189 μm, the image resolution was 1024 × 768, and the pixel size 0.246 × 0.246 μm. Basic principles of locating and identification of minerals in thin-polished sections with SEM-EDS were followed. The samples were examined in the BSE mode that allows relative differentiation between mineral phases with different chemical compositions based on the contrast in their atomic number Z (atomic number contrast) (Ebnesajjad, 2014). Atomic number Z is unique for each chemical element that constitutes the minerals and is a basis for BSE imaging. Mineral grains containing higher Z elements usually appear brighter than minerals with low Z elements (Goldstein et al., 2017). To analyze and interpret the mineral in detail, the acquisition of high-quality spectra is essential. After locating minerals grains of interest with the BSE image, the qualitative and semi-quantitative chemical composition of selected grains was measured using an energy-dispersive X-ray spectrometer (Goldstein et al., 2017). The EDS detects and processes X-rays that are emitted from constituent elements in the beam interaction volume and are characteristic of each chemical element, dependent on its atomic number. Atomic proportions of constituent elements were calculated from atomic % obtained by the semiquantitative EDS analysis, and compared to atomic proportions of constituent elements in stoichiometric minerals. X-ray intensities were converted to wt% oxides. Based on the best fit between these proportions, mineral, phases were assessed. The number of analyzed mineral grains (N) depends on the quantity of each mineral in the sample.

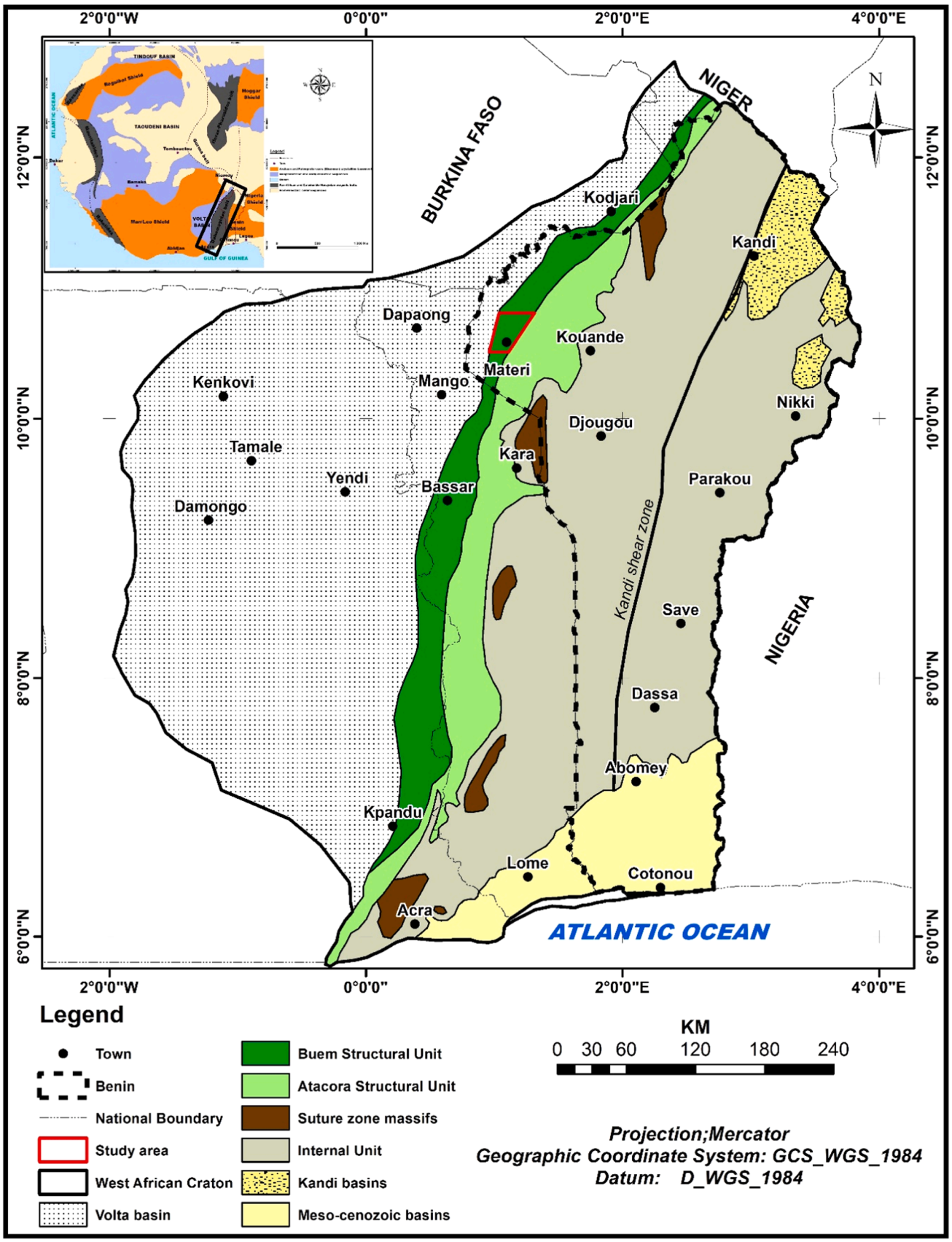

Fig. 1. Geological map of Dahomeyide orogenic belt showing the study area (in red square) and an inset map of the geology of West and North Africa showing the Dahomeyide orogenic belt (in black square), (after Affaton, 1987).

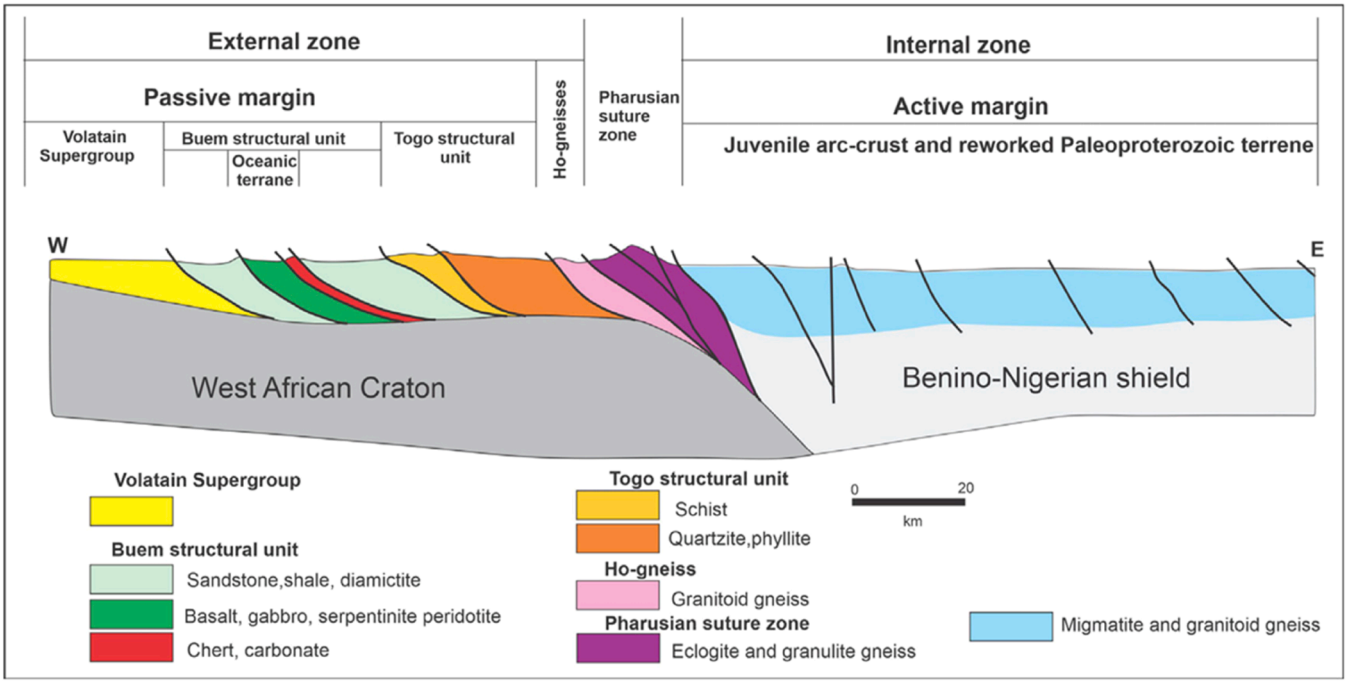

Fig. 2. Geological map of the Dahomeyide orogenic belt showing the major units and their relationship (Guillot et al., 2019).

3.2. Chromite mineral chemistry

In situ chemical analyses of chromite minerals were carried out on ten (10) polished thin sections of samples from the BSU, including chromitite (6 samples), volcanic rocks (2 metabasalts) and serpentinite (2 samples). The analyses were performed using four-channel CAMECA SX50 Electron Micro-Probe Analyser (EMPA) at the Department of Geology, University of Johannesburg in South Africa. The analyses were carried out on the Cr-spinel from BSU chromitite, metabasalt and serpentinite. The analytical conditions were 20 kV accelerating voltage, 40 nA probe current, and a beam diameter of 1 μm. The standards used for the analyses were: chromite (for Cr, Al and Fe), periclase (for Mg), rhodonite (Mn), rutile (for Ti), NiO for (Ni), and metallic V. The probe detection limits (DLs) and standard deviation for each analysis were 95 %. Fe $^{3+}$ in chromite was calculated using the charge balance equation of Droop (1987) and by re-calculating analyses to 24 cations.

3.3. Whole-rock major and trace elements analyses

Nine (09) fresh representative samples of metabasalt and serpentinite were analysed for whole rock major and trace element compositions. The selected samples were crushed, pulverized to below 200 mesh at the Department of Geology of the University of Johannesburg, South Africa. The major and trace element analyses were carried out by X-ray fluorescence and Inductively-Coupled Plasma-Mass Spectrometer (ICP-MS), respectively. Whole rock major element analysis was conducted at the Department of Geology of the University of Johannesburg, South Africa. Homogenized powder of about 0.2 g of each sample was mixed with $LiBO_2/Li_2B_4O_7$ flux after drying at 105°C. Crucibles of the mixing were fused in a furnace at 1025°C, and the cooled bead was dissolved in ACS-grade nitric acid. The solution was then analysed by X-tray fluorescence for the major element concentrations. The Loss on Ignition (LOI) was also determined by ignition of the sample split and then measuring the weight loss after 30 minutes at 930°C in the air. For trace elements analysis, the powder of the samples was packaged and sent to the Actlabs Laboratory in Ontario, Canada. The analysis was performed in accordance with the Code 4B2 Lithoresearch analytical package (Report No.: A24–05032) with detection limits ranging between 0.001 – 0.01 %.

4. Results

4.1. Field observations and petrology

The study area consists of a chain of hills trending NNE-SSW. The chromitite bodies are exposed mainly in three localities: Wantehoun in the northeastern, Sapoua and Tiélé in the central, and Kantchekohoun in the southwestern parts of the study area (Fig. 3). At Wantehoun and Sapoua they outcrop in association with serpentinite.

4.1.1. Mafic-ultramafic rocks

4.1.1.1. Serpentinite. Serpentinite is dark-green in colour and generally outcrops at the foot of hills (Fig. 4A). It is usually in contact either with metabasalt or rarely chert and shows massive to schistose texture. The rocks shows NE-SW trends and dip less than 45 degrees especially in the thrust fault zone. The serpentinite shows tectonic ductile and brittle structures as well as foliation crenulations (S2 and S3), and S-C fabrics (Fig. 4B and C). In thin section, serpentinite generally has a mesh texture to fibrous texture (Fig. 4E). It mainly contains serpentine, about 85 %; chromite and magnetite, about 10 %; and about 5 % talcose minerals. The chromite minerals are disseminated and vary in grain size (Fig. 4E).

4.1.1.2. Meta-basalt and breccias. The best exposures of meta-basalt are in the quarry sites within the study area. The rock is greyish-green and comprises massive and pillow lavas (Fig. 5A). The pillow lava ranges in diameter from 5 to 15 cm. In hand samples, these rocks show massive texture, while in thin sections they display intergranular and microlithic texture (Fig. 5B). The primary minerals are partially to wholly altered, with plagioclase altered into sericite and calcite and pyroxene into chlorite but with preserved pseudomorphs. Some opaque minerals, including chromite and magnetite, are found disseminated within the silicate minerals (Fig. 5B). Volcanic breccias are made up of various angular to subangular fragments of mafic rock and chert, ranging in size from 5 to 22 cm (Fig. 5C and D). Their texture shown various fragments within a cryptocrystalline or partial devitrified groundmass (Fig. 5E).

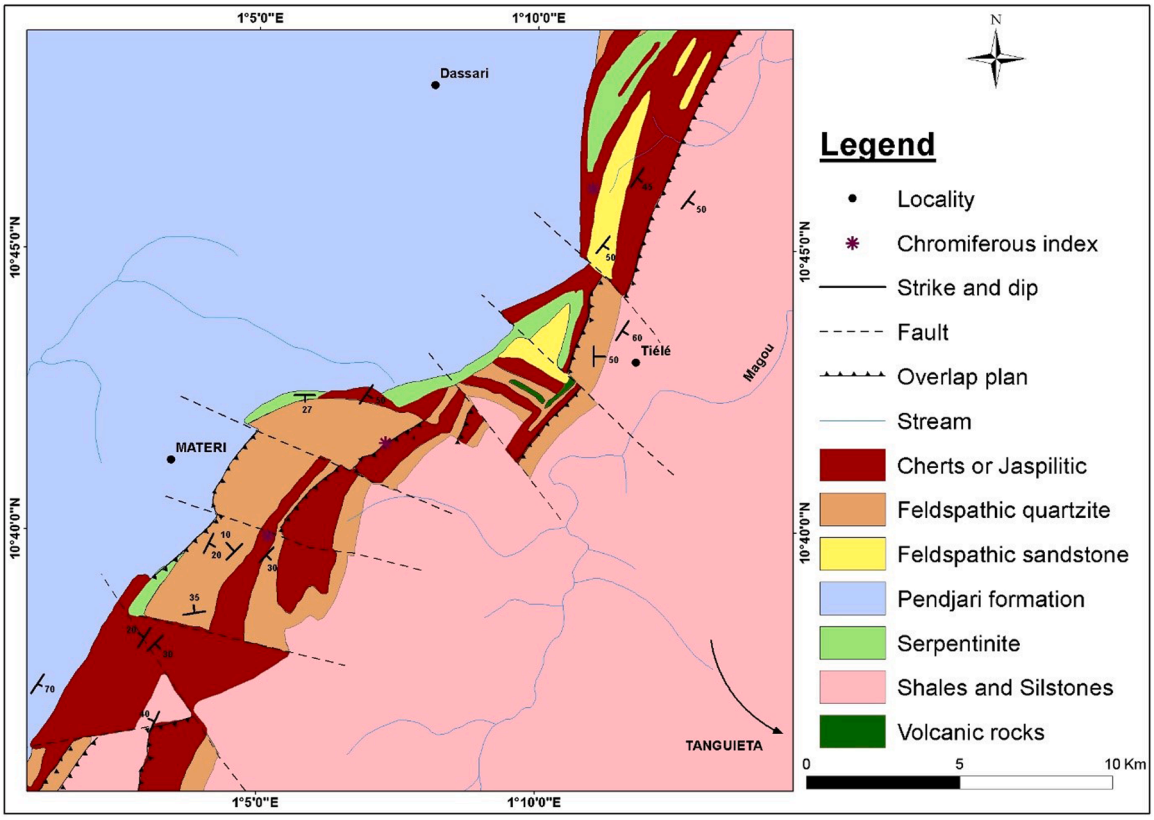

Fig. 3. Geological map of the study area (after Jébrak and Marcoux, 2008).

Thin veins (5–10 cm) of quartz cut the breccias (Fig. 5D). Chert and sandstone overlain the mafic rocks. Based on their petrographic characteristics, the mafic rocks can be categorised as porphyritic basalt or aphyric basalt. The volcanic breccia consists of auto-breccia and subordinate pyroclastic breccia.

4.1.2. Chromitite

Podiform chromitite in the Buem Structural Unit is typically lens-shaped, mainly hosted in serpentinite. The deformation structures (schistosity and fractures) of serpentinite are parallel to the chromitite bodies (Fig. 6A). According to Cassard et al. (1981) classification, the podiform chromitite of the BSU is concordant. The chromitite is massive, and exhibits pull-apart fractures and cataclastic textures. The fractures transformed chromite into a fine-grained assemblage of angular fragments within the chromitite (Fig. 7B). In transmitted light, the chromite is brownish-red (Fig. 7A-C), indicating that it is unaltered to weakly altered. In some cases, alteration zones particularly located along cracks and fractures or altered parts of some chromite edges are observed. This is also evident in reflected light by the absence of a light-coloured zone that normally corresponds to a Fe^{3+} enriched area (Fig. 7D-E). Scanning Electron Microscope observations indicate that some chromite rims are brighter suggesting the alteration of these chromite rims into ferrian chromite or magnetite (Fig. 8A). Chromite grains of chromitite contain inclusions of serpentine, quartz, chlorite, galena, iron oxides (goethite and hematite), native silver and monazite (Fig. 8B and C). Serpentine and iron oxides occur mainly in the fractures of chromitite (Fig. 8B and C). Despite the significant serpentinization, chromian spinel shows insignificant Fe^{3+} in the rims, which is often associated with late fractures in chromite minerals.

4.2. Geochemical characteristics of mafic-ultramafic rocks and chromitite

4.2.1. Geochemical characteristics of mafic-ultramafic rocks

The major (wt%) and trace (ppm) element concentrations of the studied rocks are presented in Table 1. The whole-rock analyses data of mafic-ultramafic of the BSU show that they are characterised by SiO_2 content of 37.87–45.68 wt%, Cr_2O_3 of 00–0.52 wt%, Al_2O_3 of 0.57–17.71 wt%, TiO_2 of 00–1.83w.%, CaO of 0.06–13,56 wt%, MgO of 6.49–38.59 wt%, MnO of 0.08–0.24 wt%, NaO_2 of 00–2.25 wt%, K_2O of 00–0.50 wt% and P_2O_5 of 00–0.16 wt%.

The REE element of the mafic-ultramafic rocks of the study area is plotted against chondrite -normalised Rare Earth Elements and the primitive mantle-normalised abundance for incompatible elements (Fig. 10 A and B). The REE patterns defined by these rocks are similar to the REE patterns for E-MORB and N-MORB (Fig. 10 A). Rocks that have experienced very little to no significant alteration/metamorphism are characterised by low values of Loss of Ignition (LOI) (Jiang et al., 2017; Kwayisi et al., 2022a, 2022b). However, the mafic-ultramafic rocks of BSU exhibit high LOI values ranging from 6.39 to 15.41 wt%. According to Pearce and Cann (1973) and Pearce (1975), some trace elements (Sr, Rb, and K) of the chemical composition of rocks are significantly impacted by secondary modification (alteration/metamorphism) than others (Ti, Zr, and Y) that are generally immobile. Whitford et al. (1988) highlighted that REE (especially LREE) can be mobile during hydrothermal alteration and low-grade metamorphism. To ascertain the use of the HFSE and especially the REE for petrogenetic and tectonic setting interpretations, plots of LOI versus Th/Lappm was used (Fig. 9A and B). In these figures, there is a general lack of correlation between LOI and Th/Lappm, giving compelling evidence that the primary Th-LREE concentrations in the volcanic rocks have not been disturbed by alteration or metamorphism. Hence these elements can be used to assess the petrogenesis and tectonic setting of the volcanic rocks.

Fig. 4. Field photographs showing the Buem schistose serpentinite near hill (A), crenulation of the steep S2 tectonic foliation of schistose serpentinite (B), tectonic S-C fabric recorded inserpentinite (C) serpentinization alteration of ultramafic rock (D), and microphotograph of serpentinite from Buem showing mesh texture of serpentine (Serp) and opaques (Opq) minerals (E).

4.2.2. Chemistry of chromite

Representative analyses of chromite from polished thin sections of chromitite, metabasalt and serpentinite of the BSU are given in Tables 2–4. The chemistry of chromite in the BSU chromitite and mafic-ultramafic rocks shows a wide variation. The chromitites are characterised by Cr_2O_4 contents of 38.20–43.69 wt%, Al_2O_3 of 19.82–31.87 wt %, FeO of 11.42–13.44 wt%, MgO of 14.62–18.24 wt%, MnO of 0.05–0.16 wt%, TiO_2 of 0.01–0.21 wt% and V_2O_3 of 0.11–0.18 wt%, while the chromite inclusions in mafic-ultramafic rocks have the following compositional ranges: Cr_2O_3 (35.91–43.39 wt%), Al_2O_3 (26.38–31.87 wt%), TiO_2 (0.03–0.09 wt%), MgO (12.79–16.55 wt%), MnO (0.12–0.23 wt%) and FeO (12.78–20.10 wt%) (Table 5, samples MT01 and MT24). The atomic ratio of Cr# [(Cr/Cr+Al)] of chromite ranges from 0.60 to 0.68 and is higher than mafic-ultramafic one (0.44–0.54). Similarly, Mg# [(Mg/Mg+Al)] of chromitite varying from 0.71 to 0.74 and higher than mafic-ultramafic one (0.49–0.50). The analysis data plotted on the diagrams in Fig. 11A-D shows that all chromite falls into the field of magnesiochromite (Fig. 11A) and podiform field (Fig. 11B-C), respectively.

5. Discussion

5.1. Classification and comparison of the BSU chromite composition with others

Chromite mineral chemistry investigation is useful in the study of ophiolites (Irvine, 1965, 1967; Dick and Bullen, 1984; Kamenetsky et al., 2001; Matveev and Ballhaus, 2002). As a result of the resistance of chromian spinel to alteration and metamorphic processes, its composition is often thought to represent crystallisation composition and consequently, chromite is regarded as a good petrogenetic and tectonic setting indicator (Irvine, 1967; Dick and Bullen, 1984; Arai, 1992). This is especially true for chromian spinel from chromitite, dunite and basalt flows. Cr, Al, Ti and V are the important elements for inferring the crystallisation condition of chromian spinel because of their low diffusivity (Arai and Yurimoto, 1994). The analytical data of the BSU chromite show that the chromite minerals are magnesiochromite, then indicate that they are unaltered or not significantly altered (Fig. 11A).

According to Irvine (1965) and Dick and Bullen (1984), a higher

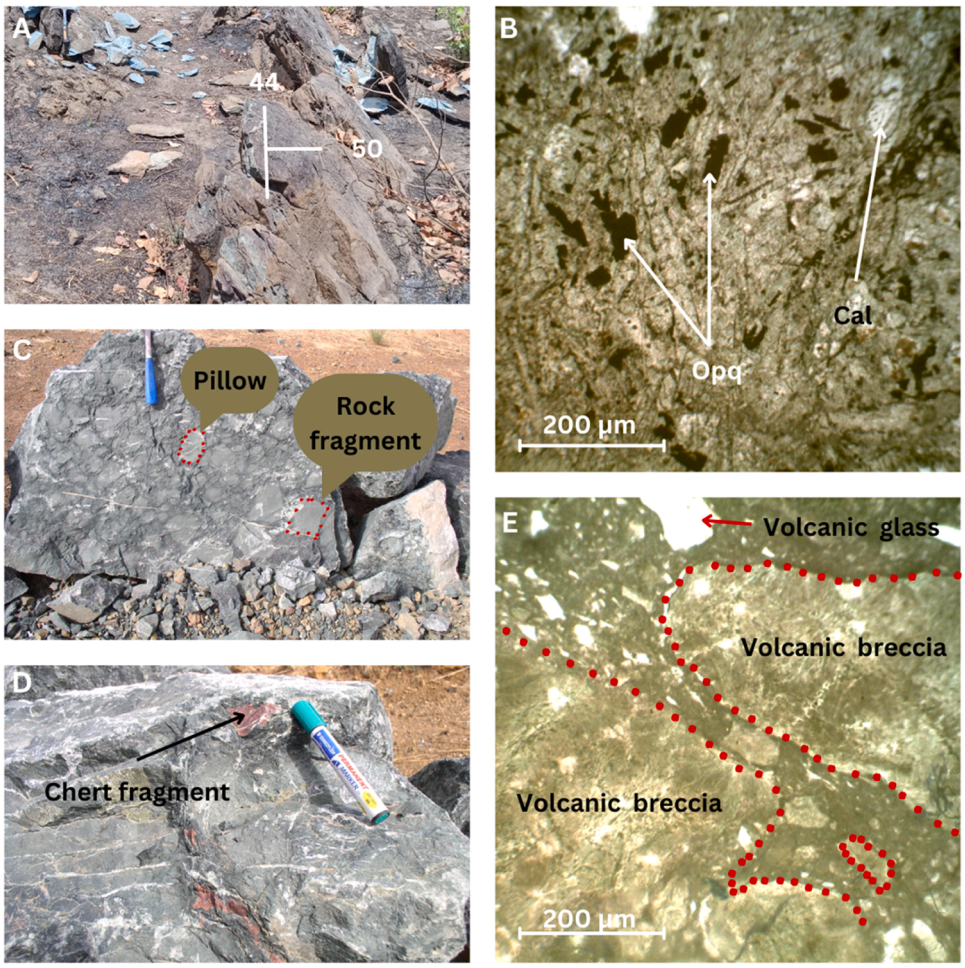

Fig. 5. Field photographs of metabasalt and breccias from Tiele within the Buem: (A) metabasalt, (C) breccias showing volcanic rock fragments, (D) breccias showing included chert fragments, (B) microphotographs of metabasalt showing altered plagioclase, calcite (Cal) and opaque (Opq) minerals and (E) and volcanic breccias microphotograph showing porphyritic texture.

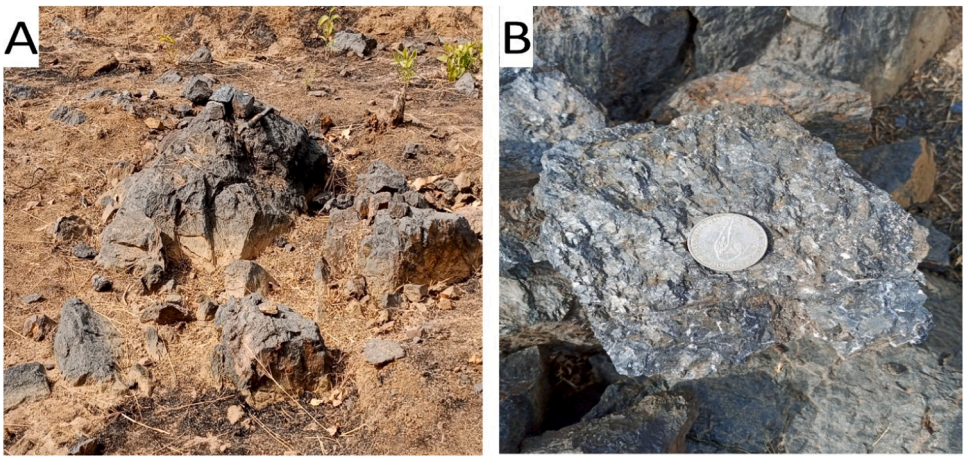

Fig. 6. Field photographs of Sapoua chromitite bodies within serpentinite in the BSU.

value of Cr# = [(Cr/Cr+Al)] indicates the degree of depletion of the mantle source from which the melt was derived. Besides, the TiO_2 wt% content can be used to assess the degree of depletion of the mantle source and the degree of melt fractionation (Shervais, 1982; Dick and Bullen, 1984; Arai, 1992; Kamenetsky et al., 2001). The vanadium content is also important in determining the degree of depletion of the mantle source, the degree of melt fractionation, and the fO_2 during partial melting, melt fractionation and chromite crystallization (Shervais, 1982). The Cr# of mantle and crust hosted chromitite is generally similar (e.g., Dick and Bullen, 1984; Orberger et al., 1995). Podiform chromitite exhibits a wide range of compositions from high-Cr to high-Al. High-Cr varieties have Cr# greater than 60, whereas the

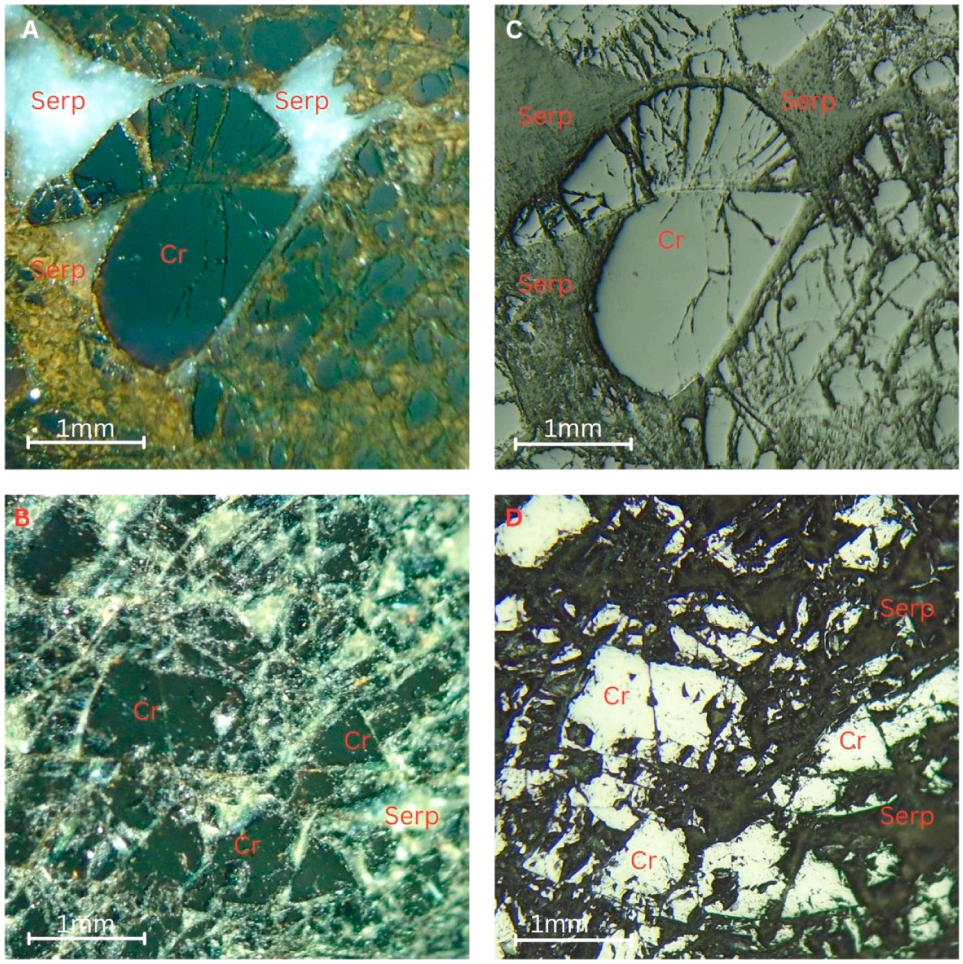

Fig. 7. Photomicrographs of the BSU chromitite in transmitted (A an B) and reflected (C and D) light showing chromite (Cr) and serpentinite (Serp) minerals.

high-Al type typically has Cr# varying between 40 and 60 (Thayer, 1964; Leblanc and Violette, 1983; Zhou and Bai, 1992). Both types are common in ophiolites, which are hosted in harzburgites and dunites of the upper mantle. The composition of parental magma appears to be the most important factor controlling chromian spinel composition, although small variations may reflect differences in temperature, pressure and oxygen fugacity (Dick and Bullen, 1984; Arai, 1992). Chromian spinel with high Cr# are thought to be formed from highly magnesian magmas (boninitic type), while those with lower Cr# precipitate from tholeiitic melts (Dick and Bullen, 1984; Arai, 1992). Magma composition is in turn, related to the degree of partial melting in the upper mantle, with high magnesian melts reflecting the highest degree of melting. Thus, the Cr-rich chomitites are interpreted as the crystallization products of magmas formed by high degrees of partial melting whereas high-Al chromitites are derived from magmas formed by lower degrees of partial melting.

In the case of the chromitite associated with the BSU, they showed moderate Cr# values (0.60–0.68). This molar ratio (Cr#) average of the chromite (Tables 2–4) is indicative of a moderate degree of mantle melting, or partial melting of previously depleted mantle source. The TiO_2 wt% content (0.01–0.21) of BSU chromite is typical of chromite from modern Mid Oceanic Ridge (MOR) setting (Dick and Bullen, 1984; Kamenetsky et al., 2001). A comparison of Cr# with TiO_2 concentration shows that within the deposit, Cr# is largely constant, whereas TiO_2 is variable. The variable TiO_2 could be explained by alteration or reflect different magma's Ti contents during chromite crystallisation.

The Cr# of chromites from different tectonic settings is distinct and reflects the differences of magma compositions from which the chromite has been formed. The primary chromites from BSU have Cr# of (0.60–0.68), are similar to those from chromitites pods hosted in depleted mantle harzburgite (with MORB affinity) of the mantle section in Wadi Rajmi, northern Oman with Cr# (0.52–0.64; Rollinson, 2008). Also, the BSU chromites are similar to those from the Mugla ophiolite, (SW Turkey), interpreted as MORB-type with Cr# (0.49–0.53; Uysal et al., 2009). In contrast, they are lower than those of boninitite formed in Supra-Subduction Zone of Rutland Island, (Andaman) with Cr# (0.73–0.80, Ghosh et al., 2009 and Cr#: 0.80–0.90; Roeder and Reynolds, 1991). The chromite of the BSU shows similar chemical characteristics (Cr#, MORB-like affinity) with those sharing the same tectonic setting (Oman and Muglan). This corroborates our interpretation that the Buem chromite probably crystalized from MORB-like magma.

5.2. Constraints on the source of the BSU mafic-ultramafic rocks and chromitite parental magmas

5.2.1. Insights on the source of the BSU mafic-ultramafic rocks

To determine the source of magma from which the mafic-ultramafic rocks of the BSU originated and the emplacement environment, plots of immobile trace elements normalised to chondrite and primitive mantle were generated (Fig. 10 A and 10B). The plots of multi-elements from magmatic rocks of BSU, against chondrite -normalised Rare Earth Elements (REE, Fig. 10 A) and the primitive mantle-normalised abundance for incompatible elements (Fig. 10B) indicate that the magmatic rocks show MORB affinity. On these plots, the meta-basalts generally display nearly flat patterns resembling MORB. This type of ridge forms when continents break up and evolve from 'rifting' to a drifting stage before a

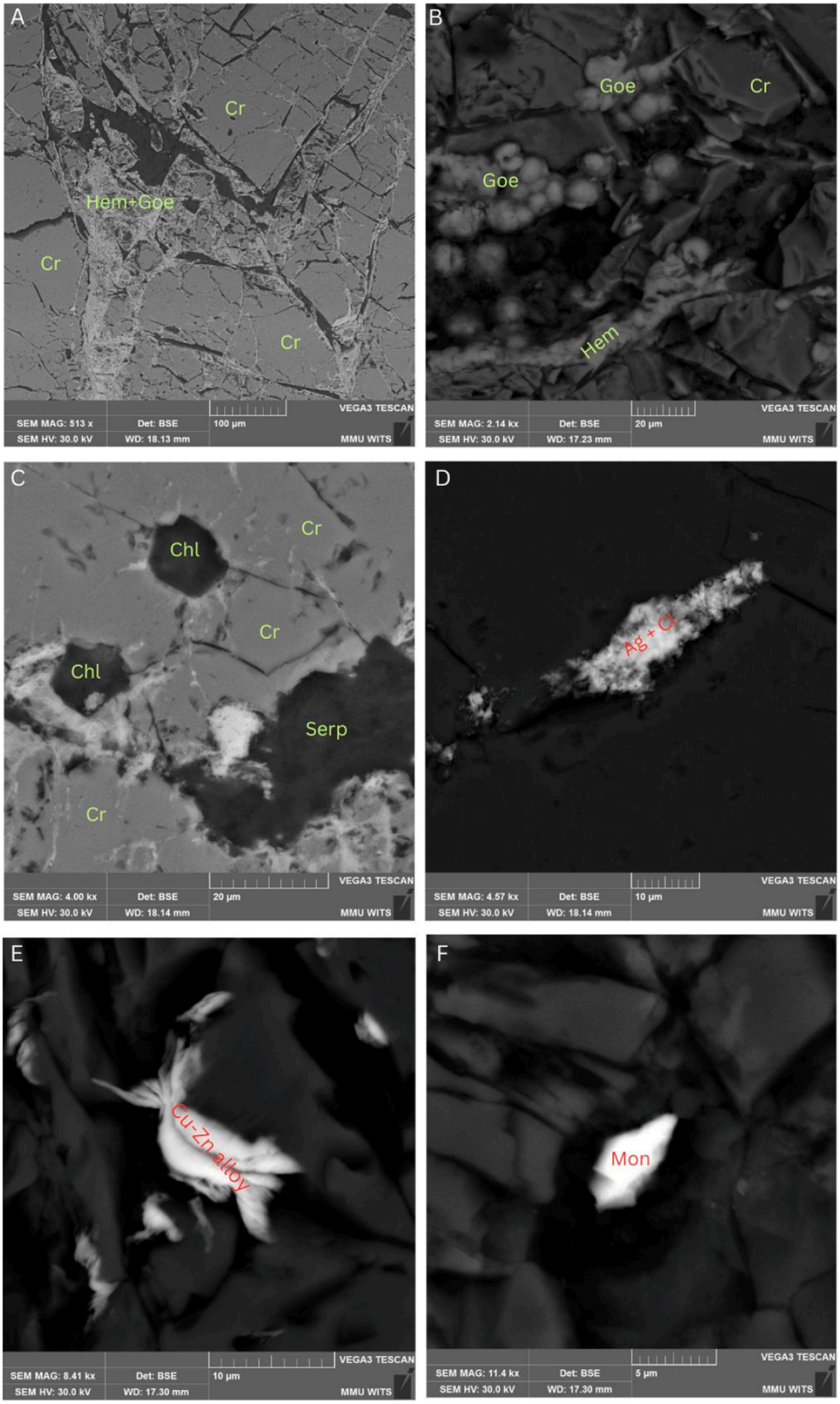

Fig. 8. Backscattered electron photomicrographs of chromite showing Cr-spinel and hematite-goethite oxides (A, B), chlorite, serpentine and Cr-spinel (C), silver-chloride (D), Cu-Zn alloy (E) and Monazite (F).

steady-state spreading regime is developed (Whitmarsh et al., 2001). In this case, the presence of cool continental lithosphere and non-infinite extension (compared to the situation once spreading is established) typically leads to cooler, shorter melting columns and hence less melting, which may, in part, at least, be responsible for the MORB character.

Table 1
Major and trace elements of mafic-ultramafic from BSU.

Sample	SPB01	MT12	MT17	MAM01	MAM02	MAM03	MT01	MT24	MT24B
SiO_2	39.72	42.57	43.5	44.79	45.68	37.87	41.17	38.85	38.67
TiO_2	-	1.45	1.31	1.26	1.24	1.83	-	-	1.31
Al_2O_3	0.63	15.2	14.07	14.89	14.51	17.71	0.97	0.57	13.22
MgO	38.59	6.49	9.49	7.12	6.92	8.31	37.48	38.01	6.72
Fe_2O_3	8.49	9.46	10.43	10.59	10.15	14.79	7.91	7.5	9.09
MnO	0.08	0.19	0.11	0.18	0.17	0.17	0.09	0.07	0.24
CaO	0.06	9.51	7.3	11.05	11.2	11.94	0.07	1.17	13.56
BaO	-	-	-	-	-	-	-	-	-
K_2O	-	0.13	0.27	0.26	0.3	0.5	-	-	0.12
Na_2O	-	2.25	2.12	2.05	2.01	0.28	-	-	1.15
NiO	0.31	-	-	-	-	-	0.4	0.3	-
P_2O_5	-	0.16	0.12	0.12	0.11	0.16	-	-	0.14
SO_3	-	0.11	0.15	0.17	0.14	-	-	-	-
Cr_2O_3	0.39	-	-	-	-	-	0.44	0.52	-
V_2O_5	-	-	0.06	0.06	0.06	0.07	-	-	-
Total	100.72	98.84	99.31	99.38	98.89	100.04	101.08	100.77	98.99
LOI	12.45	11.33	10.38	6.85	6.39	6.41	12.57	13.77	14.77
La	0.05	5.13	3.5	4.6	4.67	5.6	1.16	0.05	4.91
Ce	0.05	14.3	9.66	12.5	12.6	16.9	0.37	0.05	13.6
Pr	0.01	2.1	1.43	1.8	1.8	2.57	0.14	0.01	2
Nd	0.05	11	7.52	9.56	9.74	13.3	0.46	0.05	10.6
Sm	0.01	3.22	2.44	2.95	2.9	4.1	0.06	0.01	3.12
Eu	0.006	1.05	0.813	1	0.994	1.4	0.012	0.005	1.06
Gd	0.01	4.21	3.3	3.95	4.07	5.72	0.08	0.01	3.9
Tb	0.01	0.72	0.58	0.71	0.72	1.01	0.01	0.01	0.66
Dy	0.01	4.84	4.03	5.12	4.99	6.85	0.1	0.01	4.35
Ho	0.01	1.03	0.86	1.06	1.05	1.4	0.02	0.01	0.94
Er	0.01	3.14	2.6	3.28	3.17	4.35	0.06	0.01	2.91
Tm	0.005	0.467	0.383	0.479	0.468	0.621	0.008	0.005	0.422
Yb	0.03	3.11	2.48	3.01	2.92	4.03	0.05	0.01	2.74
Lu	0.006	0.439	0.365	0.484	0.439	0.589	0.007	0.002	0.434
Nd	0.05	5.13	3.5	4.6	4.67	5.6	1.16	0.05	4.91
Th	< 0.05	0.49	0.78	0.50	0.51	0.74	< 0.05	< 0.05	0.45

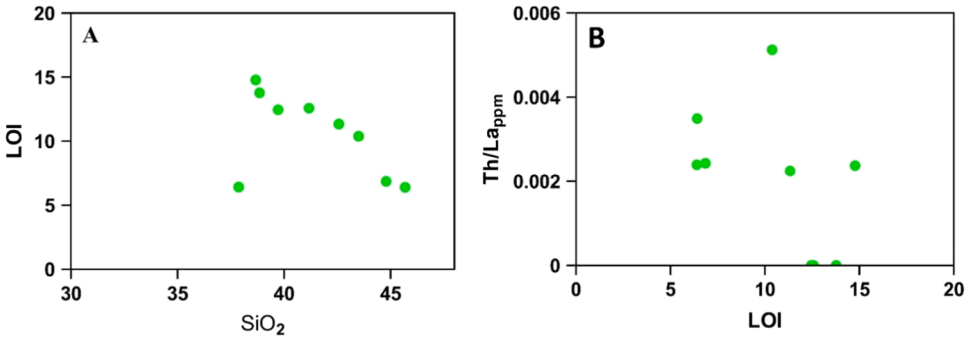

Fig. 9. plot of SiO_2 versus LOI (A) and LOI versus Th/La_{ppm} for the study area volcanic rocks (after Nude et al., 2015).

5.2.2. Constraints on the source of chromitite parental magmas

The LOI and petrography of the BSU mafic-ultramafic rocks show that these rock suites' primary major and trace element compositions might have been mobilized. This is evidenced by the serpentinization process observed in the field and the presence of secondary minerals such as serpentine, sericite, calcite and chlorite in thin sections. A plot of MnO wt% vs Cr_2O_3 wt% indicates that the chromite analyses data fall into the primary chromite field and suggest that these chromite minerals are primary chromite (Fig. 12A). The MORB affinity of BSU chromitites is also evidenced from Fe# vs Cr# plot (Fig. 12B) as the samples mostly plots close to the MORB field. Chromites from different tectonic settings have distinctive compositions based on Al_2O_3 wt% Vs TiO_2 wt% discrimination diagrams (Kelemen, 1990). BSU chromitite fall within the field of ocean ridge environment, precisely MORB-type peridotite (Fig. 12C). The Al_2O_3 wt% vs Cr_2O_3 wt% indicate that the source of parental magma of BSU chromite is the mantle (Fig. 12D). From field observations, the chert and chromitite are found as associated rock blocks in someplace. Glodji et al. (2019) interpreted this association as resulting from a tectonic process. This probably excludes chert from being primary host to chromitite unlike metabasalt and serpentinite. According to Affaton et al. (1991), the chert is formed during the Eocambrian proto-oceanisation. This is in agreement with the oceanic setting environment proposed for BSU by Affaton et al. (1997), Nude et al. (2015), and Kwayisi et al., (2022a).

It has emerged from numerous studies that the chromite is a good petrogenetic indicator. Several authors (Zhou et al., 1996; Melcher et al., 1997; Proenza et al., 1999; Uysal et al., 2007, 2009) used the chromite composition to calculate the chemical composition to calculate the melt from which it precipitated. The Al content of melt can be calculated as follows Maurel and Maurel (1982): $(AlO_3\ wt\%)_{spl} = 0.035(Al_2O_3\ wt\%)^{2.42}_{melt}$.

Because of intensive re-equilibration of Fe and Mg between chromite and silicate, the ratio FeO/ MgO of the melt from which chromite crystallized can be calculated using the following equation of Maurel (1984; cited in Uysal et al., 2007):

$$Ln(FeO/MgO)_{spl} = 0.47 - 1.07Al\#_{spl} + 0.64Fe^{3+}\#_{spl} + Ln(Fe/$$

Table 2
Representative analysis of chromite spinel from chromitite.

Sample	SP01														
Point	**1**	**2**	**3**	**4**	**5**	**6**	**7**	**8**	**9**	**10**	**11**	**12**	**13**	**14**	**15**
SiO_2	0.03	0.03	0.03	-	0.02	0.02	0.02	0.01	0.03	0.04	0.02	0.02	0.01	0.02	0.01
TiO_2	0.13	0.14	0.14	0.13	0.14	0.14	0.14	0.13	0.15	0.12	0.11	0.14	0.16	0.14	0.15
Al_2O_3	30.88	31.11	30.63	30.80	30.37	30.73	30.81	30.53	30.65	30.78	30.95	30.70	30.70	30.79	30.96
MgO	17.77	17.68	17.77	17.61	17.63	17.69	17.61	17.46	17.62	17.77	17.47	17.57	17.72	17.73	17.82
FeO	12.55	12.47	12.57	12.56	12.63	12.62	12.49	12.74	12.63	12.48	12.35	12.52	12.46	12.59	12.70
MnO	0.07	0.09	0.08	0.09	0.08	0.09	0.08	0.11	0.06	0.09	0.09	0.10	0.08	0.08	0.09
NiO	0.26	0.24	0.23	0.23	0.24	0.23	0.23	0.25	0.25	0.25	0.23	0.25	0.23	0.23	0.24
CoO	0.03	0.03	0.02	0.01	0.01	0.04	0.02	0.03	0.02	0.01	0.02	0.01	0.03	0.02	0.03
ZnO	0.06	0.04	0.04	0.05	0.03	0.04	0.03	0.05	0.05	0.04	0.05	0.05	0.05	0.02	0.04
Cr_2O_3	38.67	38.80	38.77	38.83	38.58	38.63	38.90	38.57	38.48	38.54	38.57	38.57	38.60	38.58	38.87
V_2O_3	0.15	0.15	0.15	0.18	0.14	0.14	0.16	0.15	0.17	0.16	0.15	0.15	0.15	0.14	0.15
Total	100.2	94.63	100.74	99.97	96.75	100.37	97.95	100.82	100.6	100.81	100.30	100.57	100.62	100.85	100.49
Cr	26.45	26.55	26.53	26.57	26.39	26.43	26.62	26.39	26.33	26.37	26.39	26.39	26.41	26.40	26.60
Al	16.34	16.46	16.21	16.3	16.07	16.27	16.31	16.16	16.22	16.29	16.38	16.25	16.25	16.3	16.39
Mg	10.71	10.66	10.72	10.62	10.63	10.67	10.62	10.53	10.62	10.71	10.55	10.6	10.69	10.6	10.54
Fe	9.76	9.7	9.77	9.76	9.81	9.81	9.71	9.91	9.82	9.7	9.6	9.73	9.68	9.78	9.55
Ti	0.09	0.07	0.06	0.08	0.06	0.07	0.07	0.05	0.06	0.07	0.05	0.07	0.07	0.07	0.06
V	0,1	0.1	0.1	0.12	0.09	0.09	0.11	0.1	0.11	0.11	0.1	0.1	0.1	0.1	0.1
Mn	0.05	0.07	0.06	0.07	0.06	0.07	0.06	0.08	0.05	0.07	0.07	0.08	0.00	0.07	0.07
Ni	0.21	0.19	0.18	0.18	0.19	0.18	0.18	0.19	0.2	0.2	0.18	0.2	0.18	0.19	0.18
Co	0.03	0.03	0.02	0.01	0.01	0.03	0.01	0.03	0.02	0.01	0.02	0.02	0.01	0.01	0.01
Zn	0.05	0.03	0.03	0.04	0.03	0.03	0.03	0.04	0.04	0.03	0.04	0.04	0.04	0.03	0.03
Si	0.02	0.01	0.01	-	0.01	0.01	0.01	-	0.01	0.02	0.01	0.01	-	0,01	0.01
Cr#	0.61	0.61	0.62	0.61	0.62	0.61	0.62	0.62	0.61	0.61	0.61	0.61	0.61	0.61	0.61
Al#	0.38	0.38	0.37	0.37	0.37	0.37	0.37	0.37	0.38	0.38	0.38	0.38	0.37	0.38	0.38
Mg#	0.73	0.73	0.73	0.73	0.73	0.73	0.73	0.73	0.73	0.73	0.73	0.73	0.73	0.73	0.73
Fe#	0.47	0.47	0.47	0.47	0.47	0.47	0.47	0.47	0.47	0.47	0.47	0.47	0.47	0.47	0.47
Fe^{3+} #	0.0027	0.0026	0.0027	0.0027	0.0027	0.0027	0.0026	0.0027	0.0027	0.0027	0.0026	0.0027	0.0027	0.0027	0.0027
100 *Cr#	61.81	61.72	62.07	61.97	62.15	61.89	62.01	62.02	61.88	61.81	61.70	61.89	61.90	61.82	61.87
100 *Mg#	73.72	73.74	73.69	73.53	73.44	73.52	73.63	73.08	73.43	73.83	73.70	73.54	73.80	73.45	73.82
Al_2O_3 melt	16.48	16.53	16.43	16.47	16.37	16.45	16.47	16.41	16.43	16.46	16.50	16.44	16.44	16.46	16.50
FeO/MgO melt	0.16	0.16	0.17	0.16	0.17	0.17	0.16	0.17	0.17	0.16	0.16	0.16	0.16	0.16	0.17

Fe^{3+} # = Fe^{3+} /(Cr +Al + Fe^{3+}) and Al# = Al/(Cr +Al + Fe^{3+}).

Table 3
Representative analysis of chromite spinel from chromitite.

Sample	KT01														
Point	**1**	**2**	**3**	**4**	**5**	**6**	**7**	**8**	**9**	**10**	**11**	**12**	**13**	**14**	**15**
SiO_2	0.02	0.03	0.01	0.7	0.01	0.03	0.01	0.01	-	0.01	0.02	0.01	0.01	0.02	0.01
TiO_2	0.15	0.12	0.11	0.14	0.09	0.12	0.11	0.09	0.11	0.11	0.09	0.11	0.11	0.11	0.10
Al_2O_3	30.6	28.66	29.08	19.82	29.39	29.15	29.12	28.94	29.29	29.02	29.16	29.14	28.85	28.93	29.04
MgO	17.78	17.44	17.55	17.62	17.69	17.66	17.54	17.61	17.61	17.66	17.7	17.56	17.65	17.42	17.63
FeO	12.72	12.47	12.47	12.72	12.52	12.48	12.7	12.52	12.51	12.57	12.56	12.42	12.58	12.45	12.52
MnO	0.08	0.06	0.09	0.54	0.08	0.09	0.07	0.07	0.09	0.07	0.09	0.06	0.10	0.06	0.07
NiO	0.24	0.23	0.22	0.25	0.22	0.23	0.25	0.23	0.22	0.21	0.21	0.23	0.21	0.23	0.24
CoO	0.02	0.02	0.02	0.03	0.04	0.01	0.03	0.01	0.03	0.03	0.03	0.03	0.03	0.03	0.02
ZnO	0.02	0.07	0.03	0.05	0.03	0.03	0.04	0.02	0.04	0.03	0.03	0.03	0.05	0.05	0.05
Cr_2O_3	38.63	40.85	40.65	40.88	40.57	40.66	40.77	40.64	40.52	40.76	40.79	40.73	41.03	40.68	40.64
V_2O_3	0.16	0.16	0.15	0.17	0.17	0.15	0.16	0.14	0.16	0.14	0.16	0.15	0.17	0.16	0.14
Total	100.4	100.5	99.86	99.37	100.49	100.04	100.13	100.28	100.02	100.09	100.18	100.24	100.29	100.09	100.5
Cr	26.43	27.95	27.81	32.07	27.76	27.82	27.9	27.81	27.72	27.89	27.01	27.87	28.07	27.83	27.81
Al	16.2	15.17	15.39	10.49	15.56	15.43	15.41	15.31	15.5	15.36	15.43	15.42	15.27	15.31	15.37
Mg	10.72	10.52	10.58	8.82	10.67	10.65	10.58	10.62	10.62	10.65	10.68	10.59	10.64	10.5	10.63
Fe	9.89	9.7	9.69	11.44	9.74	9.7	9.87	9.73	9.72	9.77	9.76	9.65	9.78	9.67	9.73
Ti	0.08	0.08	0.08	0.08	0.09	0.08	0.09	0.07	0.07	0.09	0.09	0.09	0.08	0.07	0.09
V	0,11	0.11	0.01	0.12	0.11	0.1	0.11	0.1	0.11	0.10	0.11	0.1	0.12	0.11	0.09
Mn	0.06	0.04	0.07	0.41	0.06	0.07	0.05	0.06	0.07	0.05	0.07	0.05	0.07	0.05	0.05
Ni	0.19	0.18	0.17	0.2	0.17	0.18	0.2	0.18	0.17	0.17	0.17	0.18	0.17	0.18	0.19
Co	0.01	0.02	0.01	0.03	0.01	0.03	0.01	0.02	0.01	0.02	0.02	0.03	0.02	0.02	0.02
Zn	0.01	0.06	0.02	0.04	0.03	0.02	0.03	0.02	0.04	0.03	0.02	0.02	0.04	0.04	0.04
Si	0.01	0.01	0.01	0.33	-	0.01	0.01	-	-	0.01	0.01	0.01	0.01	0,01	0.01
Cr#	0.64	0.64	0.64	0.64	0.64	0.65	0.64	0.64	0.62	0.62	0.62	0.62	0.62	0.62	0.62
Al#	0.37	0.35	0.35	0.24	0.35	0.35	0.35	0.35	0.35	0.35	0.36	0.35	0.35	0.35	0.35
Mg#	0.73	0.74	0.73	0.74	0.74	0.73	0.73	0.74	0.73	0.73	0.73	0.74	0.73	0.73	0.73
Fe#	0.47	0.47	0.47	0.47	0.47	0.47	0.47	0.47	0.47	0.47	0.47	0.47	0.47	0.47	0.47
Fe^{3+} #	0.0027	0.0026	0.0026	0.0027	0.0026	0.0026	0.0027	0.0026	0.0026	0.0026	0.0027	0.0026	0.0026	0.0026	0.0026
100 *Cr#	64.49	64.14	64.48	64.40	64.38	64.77	64.51	64.40	62.085	61.86	61.89	61.75	61.89	61.60	61.89
100 *Mg#	73.59	73.61	73.57	73.63	73.69	73.54	73.49	73.61	72.84	72.74	72.91	73.80	73.20	72.87	73.27
Al_2O_3 melt	16.42	15.98	16.08	13.72	16.15	16.10	16.09	16.05	16.13	16.07	16.10	16.09	16.03	16.05	16.07
FeO/MgO melt	0.17	0.18	0.18	0.3	0.18	0.18	0.18	0.18	0.18	0.18	0.18	0.18	0.18	0.18	0.18

Fe^{3+} # = Fe^{3+} /(Cr +Al + Fe^{3+}) and Al# = Al/(Cr +Al + Fe^{3+})

Table 4
Representative analysis of chromite spinel from chromitite.

Sample	MT05														
Point	**1**	**2**	**3**	**4**	**5**	**6**	**7**	**8**	**9**	**10**	**11**	**12**	**13**	**14**	**15**
SiO_2	0.03	0.02	0.02	0.01	0.03	0.02	0.02	0.01	0.02	0.01	0.02	-	0.03	0.01	0.03
TiO_2	0.19	0.18	0.18	0.18	0.19	0.17	0.19	0.17	0.18	0.17	0.18	0.18	0.18	0.19	0.17
Al_2O_3	30.65	30.83	30.74	30.98	30.79	31.1	30.64	30.93	30.84	30.54	30.59	30.95	30.41	30.6	30.49
MgO	17.64	17.59	17.52	17.59	17.52	17.3	17.6	17.5	17.59	17.47	17.67	17.58	17.44	17.58	17.55
FeO	13.03	13.06	12.9	12.37	12.71	12.76	12.72	12.55	12.87	12.76	12.81	12.56	12.87	12.05	12.96
MnO	0.08	0.08	0.10	0.9	0.12	0.11	0.09	0.12	0.10	0.12	0.12	0.10	0.10	0.12	0.10
NiO	0.24	0.24	0.22	0.23	0.23	0.24	0.22	0.22	0.24	0.23	0.22	0.23	0.24	0.22	0.23
CoO	0.03	0.01	0.02	0.02	0.03	0.03	0.01	0.01	0.03	0.01	0.03	0.04	0.04	0.04	0.03
ZnO	0.05	0.05	0.05	0.04	0.08	0.04	0.05	0.05	0.04	0.04	0.04	0.06	0.04	0.03	0.0
Cr_2O_3	38.81	38.65	38.61	38.68	38.65	38.6	38.49	38.52	38.57	38.64	38.67	38.84	38.49	38.63	38.51
V_2O_3	0.14	0.16	0.16	0.12	0.14	0.17	0.14	0.16	0.16	0.15	0.16	0.15	0.14	0.16	0.14
Total	100.9	100.87	99.51	100.3	100.5	100.54	100.19	100.25	100.64	100.13	100.51	100.7	99.29	100.96	100.63
Cr	26.56	26.45	26.42	26.46	26.45	26.41	26.34	26.35	26.39	26.44	26.46	26.58	26.33	26.43	26.35
Al	16.22	16.31	16.27	16.39	16.29	16.46	16.22	16.37	16.32	16.16	16.19	16.38	16.10	16.20	16.14
Mg	10.64	10.61	10.56	10.61	10.57	10.43	10.61	10.55	10.61	10.53	10.65	10.60	10.51	10.60	10.53
Fe	10.13	10.15	10.03	9.61	9.88	9.92	9.89	9.76	10	9.92	9.96	9.76	10	10.14	10.08
Ti	0.11	0.11	0.11	0.11	0.11	0.10	0.11	0.10	0.11	0.10	0.11	0.11	0.11	0.11	0.10
V	0,10	0.11	0.11	0.08	0.10	0.12	0.10	0.11	0.11	0.10	0.11	0.10	0.09	0.11	0.10
Mn	0.06	0.07	0.08	0.7	0.10	0.09	0.07	0.10	0.08	0.09	0.09	0.08	0.07	0.09	0.08
Ni	0.19	0.19	0.17	0.18	0.18	0.19	0.17	0.17	0.19	0.18	0.17	0.18	0.19	0.18	0.18
Co	0.03	0.01	0.02	0.02	0.03	0.02	0.01	0.01	0.03	0.01	0.02	0.04	0.03	0.03	0.02
Zn	0.04	0.04	0.04	0.03	0.06	0.03	0.04	0.04	0.03	0.03	0.03	0.03	0.03	0.04	0.04
Si	0.01	0.01	0.01	-	0.01	0.01	0.01	0.01	0.01	0.01	0.01	-	0.01	-	0.01
Cr#	0.62	0.62	0.62	0.62	0.62	0.62	0.62	0.62	0.62	0.67	0.68	0.68	0.68	0.67	0.68
Al#	0.37	0.38	0.38	0.38	0.38	0.38	0.38	0.38	0.38	0.37	0.37	0.38	0.37	0.37	0.37
Mg#	0.73	0.73	0.73	0.73	0.73	0.73	0.73	0.73	0.73	0.71	0.72	0.72	0.72	0.72	0.72
Fe#	0.48	0.48	0.48	0.48	0.48	0.48	0.48	0.48	0.48	0.48	0.48	0.48	0.48	0.48	0.48
Fe^{3+} #	0.0028	0.0028	0.0027	0.0026	0.0027	0.0027	0.0027	0.0027	0.0027	0.0027	0.0027	0.0027	0.0028	0.0026	0.0028
100 *Cr#	61.79	62.06	62.04	61.87	62.05	62.00	62.01	61.78	61.84	67.58	67.72	67.90	67.72	67.60	67.72
100 *Mg#	73.03	73.06	73.21	73.50	72.86	72.74	72.75	72.88	72.85	71.53	71.93	71.69	71.99	72.069	71.96
Al_2O_3 melt	16.43	16.47	16.45	16.51	16.46	16.53	16.43	16.50	16.48	16.41	16.42	16.50	16.38	16.42	16.40
FeO/MgO melt	0.17	0.17	0.17	0.16	0.17	0.16	0.17	0.16	0.17	0.17	0.17	0.16	0.17	0.16	0.17

Fe^{3+} # = Fe^{3+} /(Cr +Al + Fe^{3+}) and Al# = Al/(Cr +Al + Fe^{3+})

Table 5
Representative analysis of chromite spinel from chromitite (MT12) and serpentinite (MT01, MT24).

Sample	MT12												MT01		MT24	
Point	**1**	**2**	**3**	**4**	**5**	**6**	**7**	**8**	**9**	**10**	**11**	**12**	**13**	**14**	**15**	**16**
Cr_2O_3	43.12	43.38	43.69	43.04	43.24	43.2	43.33	43.27	43.18	43.22	43.58	36.42	35.91	38.09	43.39	41.37
Al_2O_3	26.74	26.74	26.7	26.53	26.79	26.63	26.64	26.73	26.96	26.49	26.52	31.37	30.87	31.87	26.38	27.26
MgO	17.03	16.97	16.69	17.02	16.89	16.88	16.83	16.91	17.07	16.89	16.62	13.81	12.79	16.55	13.81	13.74
FeO	13.43	13.12	13.06	13.12	13.97	13.03	13.44	13.43	13.87	13.15	13.31	17.94	20.10	12.78	15.71	15.44
TiO_2	0.04	0.06	0.06	0.03	0.05	0.05	0.04	0.05	0.03	0.05	0.04	0.03	0.03	0.09	0.04	0.04
V_2O_3	0.15	0.17	0.17	0.17	0.16	0.18	0.16	0.17	0.17	0.17	0.16	0.17	0.21	0.13	0.21	0.20
MnO	0.12	0.10	0.14	0.12	0.12	0.10	0.11	0.11	0.10	0.11	0.08	0.18	0.23	0.12	0.19	0.22
NiO	0.21	0.22	0.21	0.21	0.20	0.22	0.22	0.22	0.24	0.20	0.22	0.15	0.10	0.16	0.08	0.07
CoO	0.03	0.05	0.02	0.01	0.02	0.03	0.02	0.02	0.03	0.03	0.03	0.04	0.07	0.05	0.07	0.05
ZnO	0.03	0.04	0.06	0.04	0.05	0.03	0.05	0.04	0.06	0.05	0.04	0.15	0.37	0.11	0.19	0.22
SiO_2	0.01	0.01	0.01	0.02	0.1	0.03	0.01	0.01	0.02	0.07	0.01	0.02	0.04	0.02	0.03	0.02
Total	97.14	100.90	100.88	100.8	100.32	100.62	100.39	100.84	100.98	100.74	100.47	100.2	100.7	99.97	100.2	98.89
Cr	29.5	29.68	29.89	29.45	29.58	29.56	29.64	29.61	29.55	29.57	29.81	24.92	24.57	26.06	29.69	28.31
Al	14.15	14.15	14.13	14.04	14.18	14.09	14.10	14.15	14.27	14.02	14.04	16.60	16.34	16.87	13.96	14.43
Mg	10.27	10.24	10.07	10.26	10.19	10.18	10.15	10.20	10.29	10.19	10.02	8.33	7.71	9.98	8.44	8.44
Fe	10.44	10.20	10.15	10.20	10.08	10.13	10.45	10.44	10.01	10.22	10.35	13.95	15.63	9.94	12.21	12
Ti	0.02	0.04	0.03	0.02	0.03	0.03	0.02	0.03	0.02	0.03	0.03	0.02	0.02	0.05	0.02	0.03
V	0,10	0.12	0.11	0.12	0.11	0.13	0.11	0.12	0.12	0.12	0.11	0,11	0.14	0.9	0.15	0.14
Mn	0.09	0.07	0.11	0.10	0.09	0.08	0.09	0.09	0.08	0.08	0.06	0.14	0.17	0.09	0.15	0.17
Ni	0.17	0.17	0.16	0.16	0.16	0.17	0.17	0.17	0.19	0.16	0.17	0.12	0.08	0.12	0.6	0.5
Co	0.02	0.04	0.02	0.01	0.01	0.03	0.02	0.02	0.03	0.02	0.02	0.03	0.06	0.04	0.05	0.04
Zn	0.03	0.04	0.05	0.03	0.04	0.02	0.04	0.03	0.04	0.04	0.03	0.12	0.30	0.09	0.15	0.18
Si	-	0.01	0.01	0.1	0.05	0.01	-	-	0.01	0.03	-	0.01	0.02	0.01	0.01	0.01
Cr#	0.67	0.67	0.67	0.67	0.67	0.62	0.62	0.62	0.62	0.61	0.61	0.54	0.54	0.44	0.47	0.49
Al#	0.32	0.32	0.32	0.32	0.32	0.32	0.32	0.32	0.32	0.32	0.31	0.39	0.39	0.39	0.31	0.32
Mg#	0.71	0.71	0.72	0.71	0.71	0.72	0.72	0.72	0.72	0.73	0.72	0.50	0.50	0.49	0.49	0.49
Fe#	0.50	0.50	0.50	0.50	0.50	0.50	0.50	0.50	0.50	0.50	0.50	0.50	0.50	0.50	0.50	0.50
Fe^{3+} #	0.0028	0.0027	0.0027	0.0027	0.0029	0.0027	0.0028	0.0028	0.0029	0.0027	0.0028	0.0039	0.0045	0.0027	0.0033	0.0028
100 *Cr#	67.76	67.6	67.43	67.83	67.98	62.16	62.03	62.11	62.18	61.59	61.94	54.71	54.18	44.87	47.15	49.65
100 *Mg#	71.27	71.38	72.43	71.79	71.21	72.23	72.43	72.44	72.29	73.55	72.18	50.82	50	49.56	49.33	49.48
Al_2O_3 melt	15.53	15.53	15.52	15.48	15.54	15.51	15.51	15.53	15.58	15.47	15.48	16.59	16.48	16.70	15.44	15.53
FeO/MgO melt	0.22	0.21	0.21	0.21	0.23	0.21	0.22	0.22	0.22	0.21	0.22	0.23	0.26	0.16	0.26	0.22

Fe^{3+} # = Fe^{3+} /(Cr +Al + Fe^{3+}) and Al# = Al/(Cr +Al + Fe^{3+})

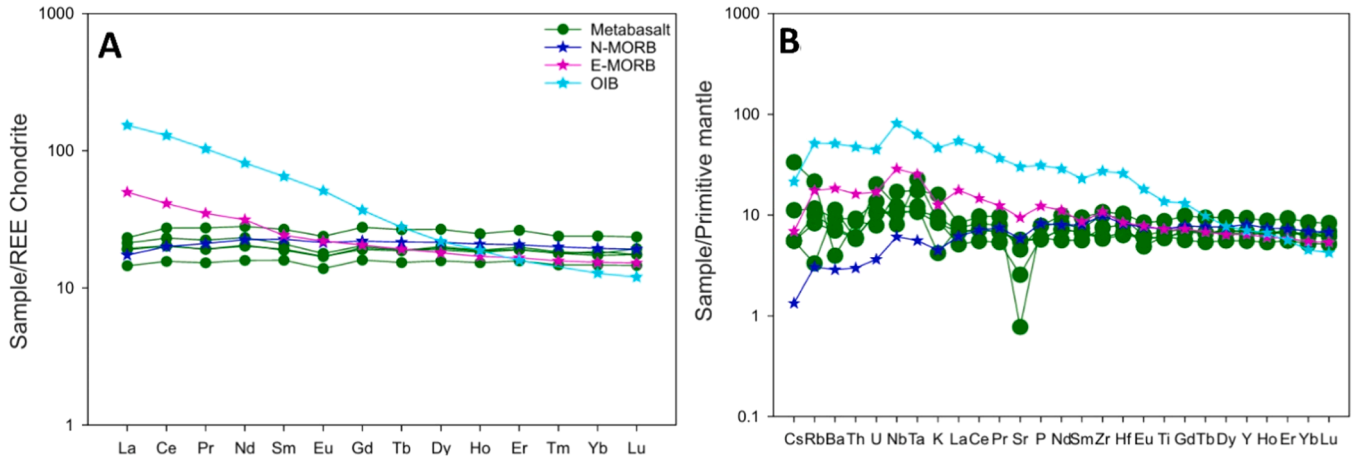

Fig. 10. chondrite-normalised REE and primitive mantle-normalised impcompatible elements of metabasalt from the BSU, (A) Chondrite-normalized REE abundance patterns (after Evensen et al. 1978) and (B) Primitive mantle-normalized abundance for incompatible elements (after Sun and McDonough, 1989) of metabasalt of the BSU.

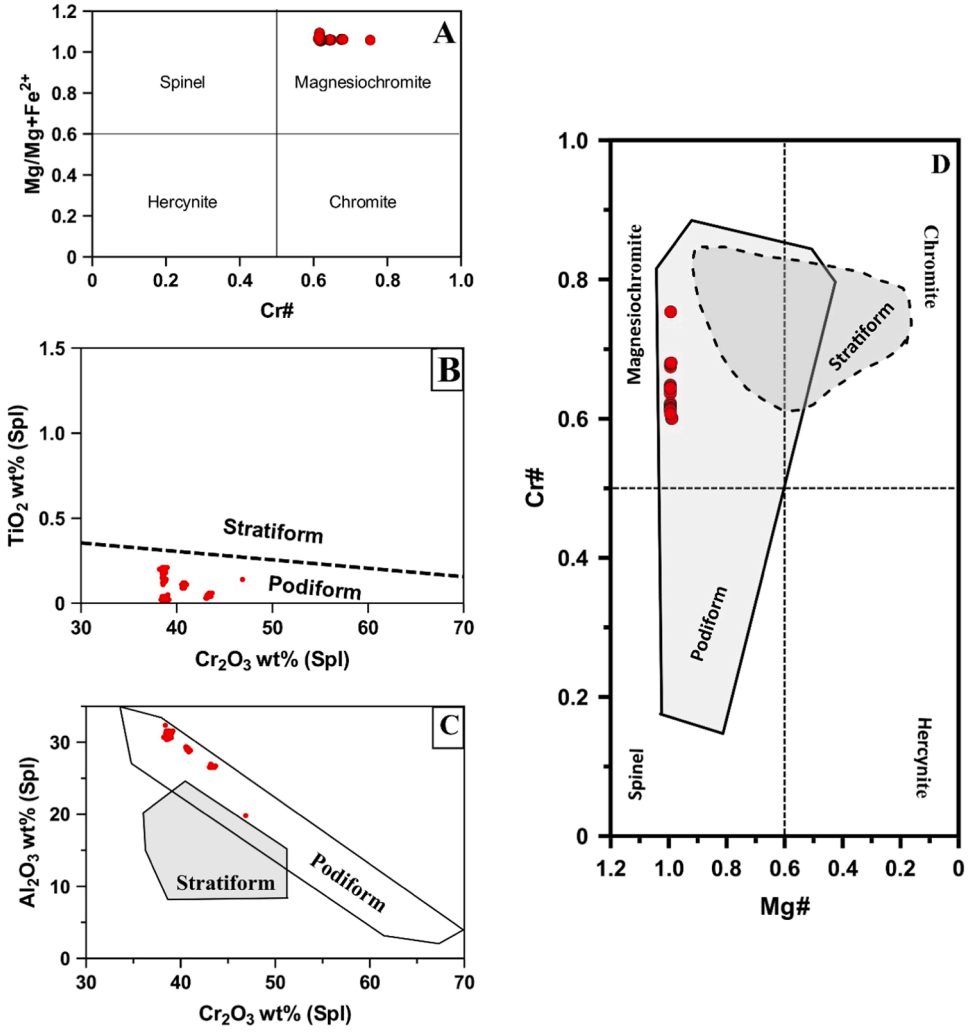

Fig. 11. Classification of BSU chromite composition plotted on (A) Cr/Cr+Al versus Mg/Mg+Fe^{2+} and (D) Mg/Mg+ Fe^{2+} versus Cr# (after Uysal et al., 2015), and plotted on (B) Cr_2O_3 versus TiO_2 (wt%) and (C) Cr_2O_3 versus Al_2O_3 (wt%) (after, Arai et al. 2004).

$MgO)_{melt}$ where Al# = Al/(Cr +Al + Fe^{3+}) and Fe^{3+} # = Fe^{3+} /(Cr +Al + Fe^{3+}). Application of these equations to the BSU chromitite gives 13.71–16.67 wt% Al2O3 and a FeO/MgO value of 0.15–0.30 for the melt from which the chromitite crystallized. The composition of the melt of the study area chromitite is higher than Kempirsia, Kazakhstan chromitite (Al_2O_3: 9.0–10.6 wt% and FeO/MgO: 0.3–0.5, Melcher et al.,

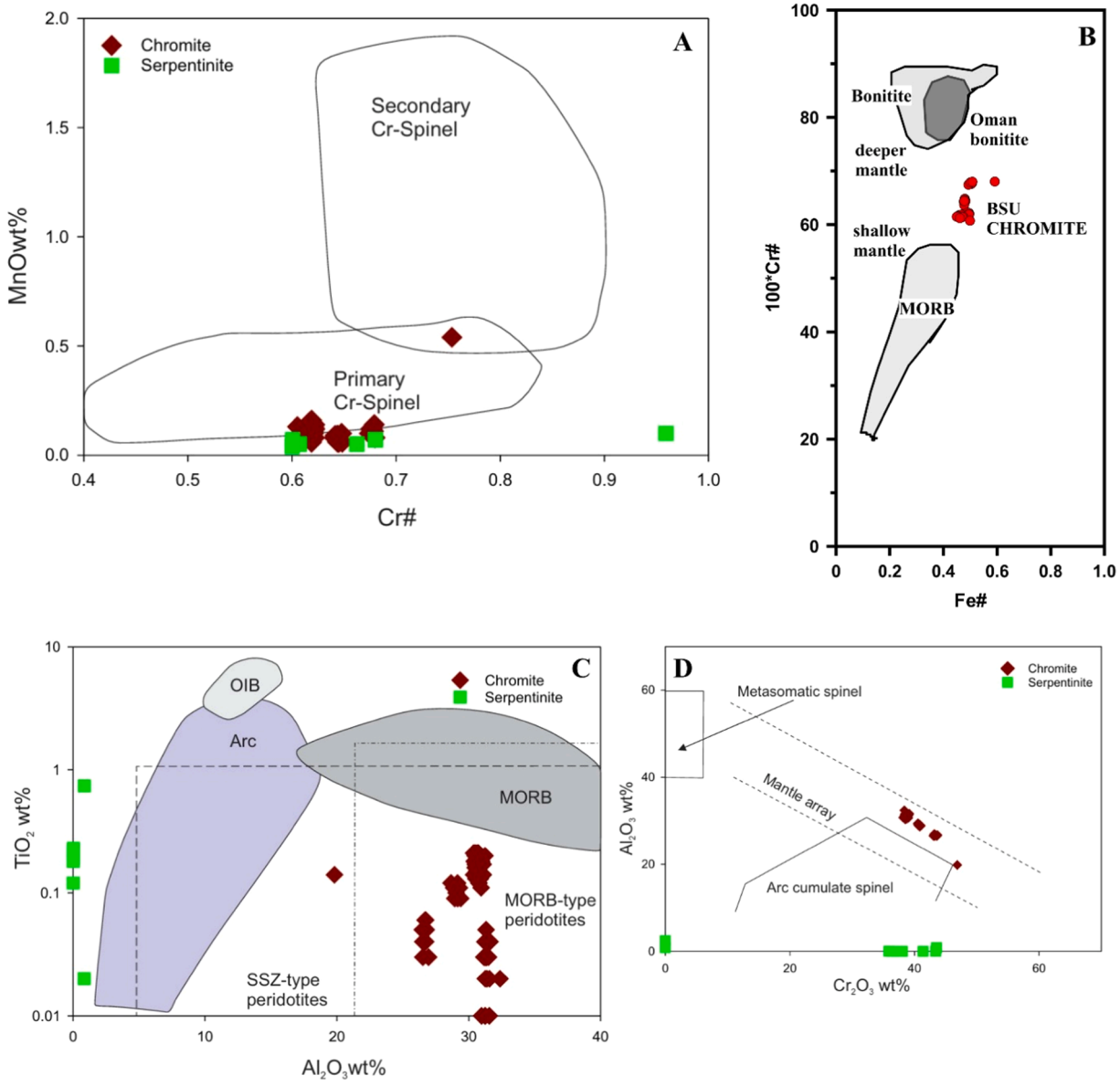

Fig. 12. Compositional range of chromian spinel in the BSU chromitite (A) Plot of MnO wt% vs Cr# for chromite (after Kepezhinskas et al., 1993), the chromite from chromitite and serpentinite plot in or close to the Primary Cr-spinel field; (B) Fe# vs 100Cr# plot for chromite (after Rollinson, 2005); (C) Plot of TiO_2 vs Al_2O_3 wt% for chromite of the Buem for the discrimination between Mid Oceanic Basalt (MORB), Oceanic Island Basalt (OIB) and Island Arc Basalt (IAB) (after Kamenetsky, 2001); (D) Cr_2O_3 vs Al_2O_3plot for chromite of the Buem (Kepezhinskas et al., 1993), chromitite spinel plot in the mantle array whereas the serpentinite spinel shows no discernable pattern.

1997), and similar to the Oman chromitite (Al_2O_3: 11.4–16.40 wt% and FeO/MgO ratio (average 0.62, Rollinson et al., 2008). The inferred composition of the melt from which the BSU chromitite precipitated is broadly similar to the composition of MORB (Al_2O_3: ~16 wt%, FeO/MgO value: 1.2–1.6 (Wilson, 1989).

5.3. Geodynamic constraints and genesis on the Buem podiform chromitite

Several models have been proposed to explain the origin of chromitite. According to González-Jiménez et al. (2011), these models can be summarised in five (5) types. The first (1) involves the cotectic crystallisation of chromite and olivine supported by mechanical separation within open conduits in the upper mantle (Lago et al., 1982; Leblanc and Ceuleneer, 1991). The second (2) model is related to the changing of fO_2 or the degree of polymerisation in the melt (McElduff and Stumpfl, 1991; Melcher et al., 1997; Proenza et al., 1999; Edwards et al., 2000). The third (3) model proposed by Béddard and Hébert (1998) suggests the formation of chromite by assimilation of preexisting mafic rocks by peridotitic intrusions. The fourth (4) model is the accumulation of chromite minerals into a water-rich fraction separated from a water-rich and co-saturated chromite-olivine basaltic melt (Matveev and Ballhaus, 2002). The fifth (5) suggests the mixing of variably differentiated (more or less silica-rich) basaltic melts within dunitic channels after melt-peridotite reactions (Arai and Yurimoto, 1994; Zhou et al., 1996; Zhou et al., 1998).

In the case of the BSU, the genesis of podiform chromitite can be linked to rifting-drifting and seafloor spreading probably during the break up of Rodinia Supercontinent. This is evidenced by the presence of pillow lavas, MORB-type trace element pattern and absence of continental fragments within serpentinite breccias in the BSU (Kwayisi et al., 2020). The pillow lavas with volcanic breccias formed during the seafloor spreading stage probably during the break-up Rodinia (Affaton et al., 1997; Nude et al., 2015; Kwayisi et al., 2022a). As proposed by

Arai and Yurimoto (1994), the rise of the upper mantle may lead to the early moderate melt of the mantle followed by the extraction of the magma from the melt which generated the volcanic rocks. During the melting of the mantle, the consumption of the orthopyroxene or pyroxene releases the co-satured chromium in the melt. The release of chromium consequently increases the chromium content in the magma. Perhaps, the ascending depleted upper mantle intruded pre-existing mafic magma or rocks (MORB type), chromite could precipitate from the assimilation of these magmas. Thus, the podiform chromite of BSU probably resulted from the assimilation of the depleted upper mantle with the adjacent mafic magma or rock. The exposures of chromitite lens shape at the contact between serpentinite and metabasalt support this argument. Also, the brittle texture of podiform chromitite and its host rocks, and the serpentinization of ultramafics suggest that chromitite formed in an oceanic setting. Further tectonic activities during the closing stages of the Buem Sea led to the integration of the BSU and the associated chromite units as ophiolite into the eastern margin of WAC.

The mafic-ultramafic rock of the BSU in Benin Republic shows several similarities (lithological and structural features) with those in the southeastern part of the Buem in Ghana (e.g, serpentinite, Affaton et al.,1997, Asiedu et al.,2008, Nude et al.,2015, Kwayisi et al., 2022a). The result from the present study combined published data on the BSU showed that this unit represents a margin-type ophiolite.

In summary, the formation of the podiform chromite of the BSU may be related to rifting-drifting and seafloor spreading probably during the break up of Rodinia Supercontinent. The BSU is an continental margin-type ophiolite.

6. Conclusion

The main conclusions of this study are:

1. Chromitite bodies occurs within the Buem Structural Unit, associated with metamorphosed ultramafic-mafic rocks now metabasalt and serpentinite. The systematic investigation of chromite from Buem revealed that they are concordant ophiolitic podiform chromitite. The chromite mineral classified as magnesiochromite and secondary silicate minerals such as serpentine, chlorite and base metal, as well as alloy (Cu-Zn), are found as inclusion in chromite spinel. The mineralogical and geochemical data are similar for chromitites in ophiolitic complexes.
2. Chromitite was precipitated from a spinel-saturated melt produced by the mixing of relatively shallow and partial melting of the mantle. It was emplaced in a mid-oceanic ridge environment most likely associated with the pre-orogenic extension event of the Dahomeyide orogeny during the Proterozoic. Otherwise, the chromites in the Buem likely crystallised from a MORB-type magma, probably derived from a depleted mantle in the passive continental margin of the West African Craton (WAC).
3. The BSU is a continental margin-type ophiolite accreted and deformed during the Pan-African orogeny.

CRediT authorship contribution statement

Samuel B.Olobaniyi: Supervision. **Luc C.Adissin Glodji:** Supervision. **Sory I.M.Konate:** Writing – review & editing. **Elhadji Mory Traore:** Writing – review & editing. **Daniel Kwayisi:** Writing – review & editing. **Clement B.N'Satta:** Writing – review & editing. **Ibrahim S. Yerima :** Writing – review & editing. **Daniel N.Kouagou N'Dah:** Writing – original draft, Conceptualization.

Declaration of Competing Interest

The authors declare that they have no known competing financial interests or personal relationships that could have appeared to influence the work reported in this paper.

Acknowledgment

This publication is part of the Ph.D. study of the first author, conducted at the University of Ibadan, Ibadan, through the Pan African University Life and Earth Sciences Institute (PAULESI), Ibadan, Nigeria. The African Union Commission provided funding for this research. Discussion and constructive comments with Professor Axel Hofmann, University of Johannesburg, South Africa, and Marina Yudovskaya, University of Witwatersrand, South Africa, gratefully acknowledged. Comments from Hugh Rollinson and Ibrahim Uysal as well as Editor Andrew Craig Kerr helped improve this paper.

Appendix A. Supporting information

Supplementary data associated with this article can be found in the online version at doi:10.1016/j.rines.2025.100080.

Data availability

Data will be made available on request.

References

Adissin Glodji, L., Bascou, J., Paquette, J.-L., Yessoufou, S., Ménot, R.-P., Amponsah, P. O., 2023. Geochronology and geochemistry of igneous rocks of the Dassa region, Central-Benin: evidence of an Ediacaran emplacement of alkali-calcic and alkaline plutonic and volcanic magmas. Int. J. Earth Sci. 112 (4), 1331–1360. https://doi.org/10.1007/s00531-023-02293-7.

Affaton, P. 1990. Le Bassin des Volta (Afrique de l'Quest): Une marge passive, du protérozoique supérieur, tectonisé au Pan-Africain (600+ 50Ma) [PhD Thesis]. ORSTOMS Paris.

Affaton, P., Aguirre, L., Ménot, R.-P., 1997. Thermal and geodynamic setting of the Buem volcanic rocks near Tiélé, Northwest Bénin, West Africa. Precambrian Res. 82 (3), 191–209. https://doi.org/10.1016/S0301-9268(97)80686-9.

Affaton, P., Rahaman, M.A., Trompette, R., Sougy, J., 1991. The dahomeyide orogen: tectonothermal evolution and relationships with the Volta Basin. In: Dallmeyer, R.D., Lécorché, J.P. (Eds.), The West African Orogens and Circum-Atlantic Correlatives. Springer, pp. 107–122. https://doi.org/10.1007/978-3-642-84153-8_6.

Agbossoumondé, Y., Guillot, S., Ménot, R.-P., 2004. Pan-African subduction–collision event evidenced by high-P coronas in metanorites from the Agou massif (southern Togo. Precambrian Res. 135 (1), 1–21. https://doi.org/10.1016/j.precamres.2004.06.005.

Agbossoumondé, Y., Ménot, R.-P., Paquette, J.L., Guillot, S., Yéssoufou, S., Perrache, C., 2007. Petrological and geochronological constraints on the origin of the Palimé–Amlamé granitoids (South Togo, West Africa): a segment of the West African Craton Paleoproterozoic margin reactivated during the Pan-African collision. Gondwana Res. 12 (4), 476–488. https://doi.org/10.1016/j.gr.2007.01.004.

Ahmed, A., Arai, S., 2002. Unexpectedly high-PGE chromitite from the deeper mantle section of the northern Oman ophiolite and its tectonic implications. Contrib. Mineral. Petrol. 143 (3), 263–278. https://doi.org/10.1007/s00410-002-0347-8.

Aidoo, F., Sun, F.-Y., Liang, T., Nude, P.M., 2020. New insight into the Dahomeyide Belt of southeastern Ghana, West Africa: evidence of arc-continental collision and Neoarchaean crustal reworking. Precambrian Res. 347, 105836. https://doi.org/10.1016/j.precamres.2020.105836.

Arai, S., 1992. Chemistry of chromian spinel in volcanic rocks as a potential guide to magma chemistry. Mineral. Mag. 56 (383), 173–184. https://doi.org/10.1180/minmag.1992.056.383.04.

Arai, S., Yurimoto, H., 1994. Podiform chromitites of the Tari-Misaka ultramafic complex, southwestern Japan, as mantle-melt interaction products. Econ. Geol. 89 (6), 1279–1288. https://doi.org/10.2113/gsecongeo.89.6.1279.

Arif, M., Qasim Jan, M., 2006. Petrotectonic significance of the chemistry of chromite in the ultramafic–mafic complexes of Pakistan. J. Asian Earth Sci. 27 (5), 628–646. https://doi.org/10.1016/j.jseaes.2005.06.004.

Asiedu, D.K., Dampare, S.B., Shibata, T., Yakubo, B.B., Osae, S., 2008. The chemical composition and significance of chromian spinels in the neoproterozoic anum serpentinites obtained from anum and dake-peki in South-Eastern Ghana. J. Ghana Sci. Assoc. 10 (1), 36–44.

Attoh, K., 1998. High-Pressure Granulite Facies Metamorphism in the Pan-African Dahomeyide Orogen, West Africa. J. Geol. 106 (2), 236–246. https://doi.org/10.1086/516019.

Attoh, K., Morgan, J., 2004. Geochemistry of high-pressure granulites from the Pan-African Dahomeyide orogen, West Africa: constraints on the origin and composition of the lower crust. J. Afr. Earth Sci. 39 (3), 201–208. https://doi.org/10.1016/j.jafrearsci.2004.07.048.

Attoh, K., Nude, P.M., 2008. Tectonic significance of carbonatite and ultrahigh-pressure rocks in the Pan-African Dahomeyide suture zone, southeastern Ghana. Geological Society, London, Special Publications, 297 (1), pp. 217–231. https://doi.org/10.1144/SP297.10.

BARNES, S.J., 2000. Chromite in Komatiites, II. Modification during greenschist to mid-amphibolite facies metamorphism. J. Petrol. 41 (3), 387–409. https://doi.org/10.1093/petrology/41.3.387.

Black, R., Latouche, L., Liégeois, J.P., Caby, R., Bertrand, J.M., 1994. Pan-African displaced terranes in the Tuareg shield (central Sahara). Geology 22 (7), 641–644. https://doi.org/10.1130/0091-7613(1994)022< 0641:PADTIT> 2.3.CO;2.

Burke, K.C., Dessauvagie, T.F.J., Whiteman, A.J., 1972. Geological history of the Benue valley and adjacent areas. Afr. Geol. 1 (8), 7–2.

CAMPBELL, I.H., MURCK, B.W., 1993. Petrology of the G and H chromitite zones in the mountain view area of the stillwater complex, Montana. J. Petrol. 34 (2), 291–316.

Cassard, D., Nicolas, A., Rabinovitch, M., Moutte, J., Leblanc, M., Prinzhofer, A., 1981. Structural classification of chromite pods in southern New Caledonia. Econ. Geol. 76 (4), 805–831. https://doi.org/10.2113/gsecongeo.76.4.805.

Chala, D., Tairou, M.S., Wenmenga, U., Kwékam, M., Affaton, P., Kalsbeek, F., Tossa, C., Houéto, A., 2015. Pan-African deformation markers in the migmatitic complexes of Parakou–Nikki (Northeast Benin). J. Afr. Earth Sci. 111, 387–398. https://doi.org/10.1016/j.jafrearsci.2015.08.009.

Dick, H.J.B., 1977. Partial melting in the Josephine Peridotite; I, The effect on mineral composition and its consequence for geobarometry and geothermometry. Am. J. Sci. 277 (7), 801–832. https://doi.org/10.2475/ajs.277.7.801.

Dick, H.J.B., Bullen, T., 1984. Chromian spinel as a petrogenetic indicator in abyssal and alpine-type peridotites and spatially associated lavas. Contrib. Mineral. Petrol. 86 (1), 54–76. https://doi.org/10.1007/BF00373711.

Ganade, C.E., Cordani, U.G., Agbossoumounde, Y., Caby, R., Basei, M.A.S., Weinberg, R. F., Sato, K., 2016. Tightening-up NE Brazil and NW Africa connections: new U–Pb/Lu–Hf zircon data of a complete plate tectonic cycle in the Dahomey belt of the West Gondwana Orogen in Togo and Benin. Precambrian Res. 276, 24–42. https://doi.org/10.1016/j.precamres.2016.01.032.

Ghosh, B., Pal, T., Bhattacharya, A., Das, D., 2009. Petrogenetic implications of ophiolitic chromite from Rutland Island, Andaman—A boninitic parentage in supra-subduction setting. Mineral. Petrol. 96 (1), 59–70. https://doi.org/10.1007/s00710-008-0039-9.

Glodji, L.A., Saïzonou, R., Adjo, F.B., Fatiou, A.K.I., Yessoufou, S., Kanon, B.A., 2019. Geology and geochemistry of the chromiferous mineralization in the external zone of the Pan-African Dahomeyides Belt, Northwestern Benin (Gulf of Guinea, West Africa). Article 12. Int. J. Geosci. 10 (12). https://doi.org/10.4236/ijg.2019.1012061.

Goldstein, J.I., Newbury, D.E., Michael, J.R., Ritchie, N.W.M., Scott, J.H.J., Joy, D.C., 2017. Scanning Electron Microscopy and X-Ray Microanalysis. Springer.

González-Jiménez, J.M., Griffin, W.L., Proenza, J.A., Gervilla, F., O'Reilly, S.Y., Akbulut, M., Pearson, N.J., Arai, S., 2014. Chromitites in ophiolites: how, where, when, why? Part II. The crystallization of chromitites. Lithos 189, 140–158. https://doi.org/10.1016/j.lithos.2013.09.008.

González-Jiménez, J.M., Proenza, J.A., Gervilla, F., Melgarejo, J.C., Blanco-Moreno, J.A., Ruiz-Sánchez, R., Griffin, W.L., 2011. High-Cr and high-Al chromitites from the Sagua de Tánamo district, Mayarí-Cristal ophiolitic massif (eastern Cuba): constraints on their origin from mineralogy and geochemistry of chromian spinel and platinum-group elements. Lithos 125 (1), 101–121. https://doi.org/10.1016/j.lithos.2011.01.016.

Irvine, T.N., 1965. Chromian spinel as a petrogenetic indicator: part 1. theory. Can. J. Earth Sci. 2 (6), 648–672. https://doi.org/10.1139/e65-046.

Irvine, T.N., 1967. Chromian spinel as a petrogenetic indicator: part 2. petrologic applications. Can. J. Earth Sci. 4 (1), 71–103. https://doi.org/10.1139/e67-004.

Jiang, Y.D., Schulmann, K., Kröner, A., Sun, M., Lexa, O., Janoušek, V., Buriánek, D., Yuan, C., Hanžl, P., 2017. Neoproterozoic-Early Paleozoic Peri-Pacific accretionary evolution of the mongolian collage system: insights from geochemical and U-Pb zircon data from the ordovician sedimentary wedge in the Mongolian Altai. Tectonics 36 (11), 2305–2331. https://doi.org/10.1002/2017TC004533.

Jiang, S.-Y., Xie, H., Ren, W., Wang, B., Yuan, F., Liu, X., Su, H.-M., 2024. Discovery and significance of layered chromite mineralization in mafic-ultramafic rocks from the Gayahe Area of the East Kunlun Orogenic Belt, Northwestern China. J. Earth Sci. 35 (4), 1367–1372. https://doi.org/10.1007/s12583-024-0041-0.

Jones, W.B., 1990. The Buem volcanic and associated sedimentary rocks, Ghana: a field and geochemical investigation. J. Afr. Earth Sci. 11 (3), 373–383. https://doi.org/10.1016/0899-5362(90)90016-8.

Kalsbeek, F., Affaton, P., Ekwueme, B., Frei, R., Thrane, K., 2012. Geochronology of granitoid and metasedimentary rocks from Togo and Benin, West Africa: comparisons with NE Brazil. Precambrian Res. 196–197, 218–233. https://doi.org/10.1016/j.precamres.2011.12.006.

Kalsbeek, F., Frei, D., Affaton, P., 2008. Constraints on provenance, stratigraphic correlation and structural context of the Volta basin, Ghana, from detrital zircon geochronology: an Amazonian connection? Sediment. Geol. 212 (1), 86–95. https://doi.org/10.1016/j.sedgeo.2008.10.005.

Kamenetsky, V.S., Crawford, A.J., Meffre, S., 2001. Factors controlling chemistry of magmatic spinel: an empirical study of associated olivine, cr-spinel and melt inclusions from primitive rocks. J. Petrol. 42 (4), 655–671. https://doi.org/10.1093/petrology/42.4.655.

Kelemen, P.B., 1990. Reaction between ultramafic rock and fractionating basaltic magma I. Phase Relations, the origin of calc-alkaline magma series, and the formation of discordant dunite. J. Petrol. 31 (1), 51–98. https://doi.org/10.1093/petrology/31.1.51.

Kwayisi, D., Agra, N.A., Dampare, S.B., Asiedu, D.K., Amponsah, P.O., Nude, P.M., 2017. Two suites of gabbros in the Buem Structural Unit, of the Pan-African Dahomeyide orogen, southeastern Ghana: constraints from new field and geochemical data. J. Afr. Earth Sci. 129, 45–55. https://doi.org/10.1016/j.jafrearsci.2016.12.018.

Kwayisi, D., Elburg, M., Lehmann, J., 2022a. Preserved ancient oceanic lithosphere within the Buem structural unit at the eastern margin of the West African Craton. Lithos 410–411, 106585. https://doi.org/10.1016/j.lithos.2021.106585.

Kwayisi, D., Lehmann, J., Elburg, M., 2020. The architecture of the Buem structural unit: implications for the tectonic evolution of the Pan-African Dahomeyide Orogen, West Africa. Precambrian Res. 338, 105568. https://doi.org/10.1016/j.precamres.2019.105568.

Kwayisi, D., Lehmann, J., Elburg, M., 2022b. Provenance and depositional setting of the Buem structural unit (Ghana): implications for the paleogeographic reconstruction of the West African and Amazonian cratons in Rodinia. Gondwana Res. 109, 183–204. https://doi.org/10.1016/j.gr.2022.04.020.

Kwayisi, D., Nyavor, E., Dzikunoo, E.A., Fynn, I.E.M., Kutu, J., Nude, P.M., 2023. Cryogenian-Ediacaran crustal growth and evolution of the active margin of the Dahomeyide belt, Ghana. Geol. Mag. 160 (10), 1914–1931. https://doi.org/10.1017/S0016756823000808.

Lago, B.L., Rabinowicz, M., Nicolas, A., 1982. Podiform chromite ore bodies: a genetic model. J. Petrol. 23 (1), 103–125. https://doi.org/10.1093/petrology/23.1.103.

Latypov, R., Chistyakova, S., Mukherjee, R., 2017. A novel hypothesis for origin of massive chromitites in the bushveld igneous complex. J. Petrol. 58 (10), 1899–1940. https://doi.org/10.1093/petrology/egx077.

Leblanc, M., Ceuleneer, G., 1991. Chromite crystallization in a multicellular magma flow: evidence from a chromitite dike in the Oman ophiolite. Lithos 27 (4), 231–257. https://doi.org/10.1016/0024-4937(91)90002-3.

Leblanc, M., Violette, J.-F., 1983. Distribution of aluminum-rich and chromium-rich chromite pods in ophiolite peridotites. Econ. Geol. 78 (2), 293–301. https://doi.org/10.2113/gsecongeo.78.2.293.

Maier, W.D., Määttää, S., Yang, S., Oberthür, T., Lahaye, Y., Huhma, H., Barnes, S.-J., 2015. Composition of the ultramafic–mafic contact interval of the Great Dyke of Zimbabwe at Ngezi mine: comparisons to the Bushveld Complex and implications for the origin of the PGE reefs. Lithos 238, 207–222.

Malkani, M.S., Alyani, M.I., Khosa, M.H., Somro, N., Arif, S.J., Tariq, S., Saeed, F., Khan, G., Faiz, J., 2016. Mineral resources of Pakistan—An update. Lasbela University Journal of Science and Technology, 5, 90–114.

Matveev, S., Ballhaus, C., 2002. Role of water in the origin of podiform chromitite deposits. Earth Planet. Sci. Lett. 203 (1), 235–243. https://doi.org/10.1016/S0012-821X(02)00860-9.

Maurel, C., & Maurel, P. (1982). Étude expérimentale de la distribution de l'aluminium entre bain silicaté basique et spinelle chromifère. Implications pétrogénétiques: Teneur en chrome des spinelles. https://doi.org/10.3406/bulmi.1982.7605.

McElduff, B., Stumpfl, E.F., 1991. The chromite deposits of the Troodos complex, cyprus—evidence for the role of a fluid phase accompanying chromite formation. Miner. Depos. 26 (4), 307–318. https://doi.org/10.1007/BF00191079.

Mekhonoshin, A.S., Kolotilina, T.B., Doroshkov, A.A., Pikiner, E.E., 2020. Compositional Variations of Cr-Spinel in High-Mg Intrusions of the Primorsky Ridge (Western Baikal Region, Russia). Article 7 Minerals 10 (7). https://doi.org/10.3390/min10070608.

Melcher, F., Grum, W., Simon, G., Thalhammer, T.V., Stumpfl, E.F., 1997. Petrogenesis of the Ophiolitic Giant Chromite Deposits of Kempirsai, Kazakhstan: a study of solid and fluid inclusions in chromite. J. Petrol. 38 (10), 1419–1458. https://doi.org/10.1093/petroj/38.10.1419.

Menot, R.P., 1980. Les massifs basiques et ultrabasiques de la zone mobile pan-africaine au Ghana, Togo et Benin; etat de la question. Bull. De. La Soci. été Géologique De. Fr. S7-XXII (3), 297–303. https://doi.org/10.2113/gssgfbull.S7-XXII.3.297.

Miura, M., Arai, S., Ahmed, A.H., Mizukami, T., Okuno, M., Yamamoto, S., 2012. Podiform chromitite classification revisited: a comparison of discordant and concordant chromitite pods from Wadi Hilti, northern Oman ophiolite. J. Asian Earth Sci. 59, 52–61. https://doi.org/10.1016/j.jseaes.2012.05.008.

Mukherjee, R., Mondal, S.K., Rosing, M.T., Frei, R., 2010. Compositional variations in the Mesoarchean chromites of the Nuggihalli schist belt, Western Dharwar Craton (India): potential parental melts and implications for tectonic setting. Contrib. Mineral. Petrol. 160 (6), 865–885. https://doi.org/10.1007/s00410-010-0511-5.

Nude, P.M., Kwayisi, D., Taki, N.A., Kutu, J.M., Anani, C.Y., Banoeng-Yakubo, B., Asiedu, D.K., 2015. Petrography and chemical evidence for multi-stage emplacement of western Buem volcanic rocks in the Dahomeyide orogenic belt, southeastern Ghana, West Africa. J. Afr. Earth Sci. 112, 314–327. https://doi.org/10.1016/j.jafrearsci.2015.09.019.

Osae, S., Asiedu, D.K., Banoeng-Yakubo, B., Koeberl, C., Dampare, S.B., 2006. Provenance and tectonic setting of Late Proterozoic Buem sandstones of southeastern Ghana: evidence from geochemistry and detrital modes. J. Afr. Earth Sci. 44 (1), 85–96. https://doi.org/10.1016/j.jafrearsci.2005.11.009.

Paktunc, A.D., 1990. Origin of podiform chromite deposits by multistage melting, melt segregation and magma mixing in the upper mantle. Ore Geol. Rev. 5 (3), 211–222. https://doi.org/10.1016/0169-1368(90)90011-B.

Pearce, J.A., 1975. Basalt geochemistry used to investigate past tectonic environments on Cyprus. Tectonophysics 25 (1), 41–67. https://doi.org/10.1016/0040-1951(75)90010-4.

Pearce, J.A., Cann, J.R., 1973. Tectonic setting of basic volcanic rocks determined using trace element analyses. Earth Planet. Sci. Lett. 19 (2), 290–300. https://doi.org/10.1016/0012-821X(73)90129-5.

Proenza, J., Gervilla, F., Melgarejo, J., Bodinier, J.-L., 1999. Al- and Cr-rich chromitites from the Mayari-Baracoa ophiolitic belt (eastern Cuba); consequence of interaction between volatile-rich melts and peridotites in suprasubduction mantle. Econ. Geol. 94 (4), 547–566. https://doi.org/10.2113/gsecongeo.94.4.547.

Roeder, P.L., Reynolds, I., 1991. Crystallization of chromite and chromium solubility in basaltic melts. J. Petrol. 32 (5), 909–934. https://doi.org/10.1093/petrology/32.5.909.

Rollinson, H.R., 2005. Chromite in the mantle section of the Oman ophiolite: a new genetic model. Isl. Arc 14, 542–550.
Rollinson, H., 2008. The geochemistry of mantle chromitites from the northern part of the Oman ophiolite: inferred parental melt compositions. Contrib. Mineral. Petrol. 156 (3), 273–288. https://doi.org/10.1007/s00410-008-0284-2.
Scowen, P.A.H., Roeder, P.L., Helz, R.T., 1991. Reequilibration of chromite within Kilauea Iki lava lake, Hawaii. Contrib. Mineral. Petrol. 107 (1), 8–20. https://doi.org/10.1007/BF00311181.
Shervais, J.W., 1982. Ti-V plots and the petrogenesis of modern and ophiolitic lavas. Earth Planet. Sci. Lett. 59 (1), 101–118. https://doi.org/10.1016/0012-821X(82)90120-0.
Spandler, C., Mavrogenes, J., Arculus, R., 2005. Origin of chromitites in layered intrusions: evidence from chromite-hosted melt inclusions from the Stillwater Complex. Geology 33 (11), 893–896. https://doi.org/10.1130/G21912.1.
Stowe, C.W., 1994. Compositions and tectonic settings of chromite deposits through time. Econ. Geol. 89 (3), 528–546. https://doi.org/10.2113/gsecongeo.89.3.528.
Tesalina, S.G., Nimis, P., Augé, T., Zaykov, V.V., 2003. Origin of chromite in mafic–ultramafic-hosted hydrothermal massive sulfides from the Main Uralian Fault, South Urals, Russia. Lithos 70 (1), 39–59. https://doi.org/10.1016/S0024-4937(03)00090-2.
Thayer, T.P., 1964. Principal features and origin of podiform chromite deposits, and some observations on the Guelman-Soridag District, Turkey. Econ. Geol. 59 (8), 1497–1524. https://doi.org/10.2113/gsecongeo.59.8.1497.
Uysal, İ., Tarkian, M., Sadiklar, M.B., Şen, C., 2007. Platinum-group-element geochemistry and mineralogy of ophiolitic chromitites from the Kop Mountains, Northeastern Turkey. Can. Mineral. 45 (2), 355–377. https://doi.org/10.2113/gscanmin.45.2.355.
Uysal, I., Zaccarini, F., Sadiklar, M.B., Tarkian, M., Thalhammer, O.A.R., Garuti, G., 2009. The podiform chromitites in the Dagküplü and Kavak mines, Eskisehir ophiolite (NW-Turkey): genetic implications of mineralogical and geochemical data. Geol. Acta 7, 351–362. https://doi.org/10.1344/105.000001442.
Whitford, D.J., Korsch, M.J., Porritt, P.M., Craven, S.J., 1988. Rare-earth element mobility around the volcanogenic polymentallic massive sulfide deposit at Que River, Tasmania, Australia. Chem. Geol. 68 (1), 105–119. https://doi.org/10.1016/0009-2541(88)90090-3.
Whitmarsh, R.B., Manatschal, G., Minshull, T.A., 2001. Evolution of magma-poor continental margins from rifting to seafloor spreading. Nature 413 (6852), 150–154. https://doi.org/10.1038/35093085.
Wilson, M. 1989. 1.989. Igneous petrogenesis. A global tectonic approach. London, UK, Unwin Hyman, Https://Doi. Org/10, 1007, 978–1.
Xiong, F., Zoheir, B., Li, C., Xu, X., Qiu, T., Benaouda, R., Chen, J., 2023. Atypical chromitite deposit in the Gaositai mafic-ultramafic complex, North China Craton: geochemical, geochronological, and isotopic systematics. Lithos 460–461, 107388. https://doi.org/10.1016/j.lithos.2023.107388.
Yang, J., Lian, D., Wu, W., 2022. Chromitites in ophiolites: questions and thoughts. Acta Geol. Sin. a 96 (5), 1608–1634.
Yang, J., Meng, F., Xu, X., Robinson, P.T., Dilek, Y., Makeyev, A.B., Wirth, R., Wiedenbeck, M., Cliff, J., 2015. Diamonds, native elements and metal alloys from chromitites of the Ray-Iz ophiolite of the Polar Urals. Gondwana Res. 27 (2), 459–485.
Zaccarini, F., Garuti, G., Proenza, J.A., Campos, L., Thalhammer, O.A., Aiglsperger, T., Lewis, J.F., 2011. Chromite and platinum group elements mineralization in the Santa Elena Ultramafic Nappe (Costa Rica): geodynamic implications. Geol. Acta. Int. Earth Sci. J. 9 (3–4), 407–423.
Zhou, M.-F., Bai, W.-J., 1992. Chromite deposits in China and their origin. Miner. Depos. 27 (3), 192–199. https://doi.org/10.1007/BF00202542.
Zhou, M.F., Robinson, P.T., Bai, W.J., 1994. Formation of podiform chromitites by melt/rock interaction in the upper mantle. Miner. Depos. 29 (1), 98–101. https://doi.org/10.1007/BF03326400.
Zhou, M.-F., Robinson, P.T., Malpas, J., LI, Z., 1996. Podiform chromitites in the luobusa ophiolite (Southern Tibet): implications for melt-rock interaction and chromite segregation in the Upper Mantle. J. Petrol. 37 (1), 3–21. https://doi.org/10.1093/petrology/37.1.3.
Zhou, M.-F., Robinson, P.T., Su, B.-X., Gao, J.-F., Li, J.-W., Yang, J.-S., Malpas, J., 2014. Compositions of chromite, associated minerals, and parental magmas of podiform chromite deposits: the role of slab contamination of asthenospheric melts in suprasubduction zone environments. Gondwana Res. 26 (1), 262–283. https://doi.org/10.1016/j.gr.2013.12.011.
Zhou, M.-F., Sun, M., Keays, R.R., Kerrich, R.W., 1998. Controls on platinum-group elemental distributions of podiform chromitites: a case study of high-Cr and high-Al chromitites from chinese orogenic belts. Geochim. Et. Cosmochim. Acta 62 (4), 677–688. https://doi.org/10.1016/S0016-7037(97)00382-7.